High Temperature Corrosion of Materials (2026) 103:28
https://doi.org/10.1007/s11085-026-10379-1

RESEARCH

High-Temperature Oxidation Behaviors of Structural Materials for Very High Temperature Reactors

Hakan Us[1] · Tushar K. Ghosh[2] · Sudarshan Loyalka[2]

Received: 7 November 2025 / Revised: 29 January 2026 / Accepted: 1 March 2026 /
Published online: 27 March 2026

Abstract

The high-temperature oxidation behavior of 316L stainless steel, Alloy 617, and Incoloy 800H—candidate structural materials for advanced energy systems—was systematically investigated in a dry air environment over a wide temperature range relevant to very high temperature reactor (VHTR) applications. Oxidation kinetics were evaluated using thermogravimetric analysis (TGA), while oxide scale morphology, elemental distribution, and phase evolution were characterized by scanning electron microscopy with energy-dispersive X-ray spectroscopy (SEM/EDS) and X-ray diffraction (XRD), respectively. The results demonstrate that oxidation behavior is strongly temperature dependent and differs significantly among the investigated alloys. 316L stainless steel exhibits the poorest oxidation resistance, characterized by the formation of porous and poorly adherent Fe-rich oxides (Fe_2O_3 and Fe_3O_4) and severe scale degradation at elevated temperatures. Incoloy 800H shows intermediate oxidation performance, forming a protective Cr_2O_3-based scale at temperatures up to approximately 1173 K; however, this protection deteriorates at higher temperatures due to chromium depletion and the increasing dominance of Fe-rich oxides. Alloy 617 forms a continuous and chromia-dominated oxide scale over a broader temperature range, resulting in lower oxidation rates and improved scale stability under the investigated conditions. Parabolic oxidation rate constants were quantitatively determined, confirming predominantly diffusion-controlled oxidation kinetics within the parabolic regime. Arrhenius analysis revealed distinct apparent activation energies for the three alloys, reflecting differences in the temperature sensitivity of oxidation processes. However, the results also indicate that activation energy alone does not directly represent overall oxidation resistance, which is strongly influenced by oxide scale morphology, adhesion, and phase stability. Based on a combined assessment of oxidation kinetics, microstructural evolution, and phase analysis, the oxidation resistance ranking under the specific dry air and short-term isothermal conditions investigated is determined to be Alloy 617 > Incoloy 800H > 316L stainless steel. These results provide a comparative assessment of high-temperature oxidation behavior under controlled dry air conditions.

Extended author information available on the last page of the article

Keywords 316L stainless steel · Alloy 617 · Incoloy 800H · High-temperature oxidation · VHTR

Introduction

High-temperature structural materials are essential for the safe and efficient operation of advanced energy systems, particularly Generation IV nuclear reactors, especially very high temperature reactors (VHTR) [1–3]. These systems are expected to expreience extreme conditions, including elevated temperatures, great neutron irradiation, and chemically aggressive environments. Under such difficult service conditions, the corrosion and oxidation behavior of structural alloys largely determines their long-term integrity, reliability, and general performance.

Austenitic stainless steels, nickel-based superalloys, and Fe–Ni–Cr alloys have been generally studied as leading candidates for structural components due to their high mechanical strength, creep resistance, and corrosion resistance [4–6]. Among these, 316L stainless steel, Alloy 617, and Incoloy 800H stand out for their potential applications in intermediate heat exchangers, pressure vessel internals, and heat transport systems, hot gas ducts, and reactor internals[7–9]. Each alloy offers unique advantages: 316L stainless steel exhibits excellent welding capability and resistance to aqueous corrosion; Alloy 617 demonstrates superior creep strength and oxidation resistance at very high temperatures; and Incoloy 800H provides good microstructural stability and carburization resistance in oxidizing environments.

The oxidation behavior of 316L stainless steel depends on factors such as temperature, oxidizing environment/surface, alloy composition, and time. The oxidation of austenitic stainless steel has already been studied by various researchers depending on alloy composition, oxidizing environment, temperature, and time [10–17]. These studies demonstrate that such steels can form a stable, dense, continuous, adhesive, and protective oxide layer composed of various oxides. Recent research shows that the oxidation kinetics of austenitic stainless steel and 316 stainless steel (316-SS) follow a parabolic law at high temperatures.[18–20].

Several nickel (Ni)-based alloys are being seriously evaluated as high-temperature structural materials[21–24] Ni-based alloys are important candidate materials for very high-temperature gas-cooled reactors (VHTRs) due to their high-temperature creep resistance, oxidation resistance, and excellent material properties—namely, phase stability and superior performance in high-efficiency systems. These alloys are widely used in many high-temperature reactors.[25]. Currently, Ni-based alloys, particularly Alloy 617 and other Ni-based alloys, are considered for intermediate heat exchangers (IHX) and hot gas ducts (HGD). This is because these alloys possess excellent high-temperature corrosion resistance against various environments such as oxidation, carburization, and decarburization.[26, 27]. In these materials, the protective outer layer of chromium oxide (Cr_2O_3) prevents direct interaction between the metal and its surroundings. [28]. Chromium (Cr) and aluminum (Al) are added to the alloy to promote the formation of an oxide layer on the surface,

thereby providing protection against degradation (oxidation and corrosion) at high temperatures. [29–31].

Among the various materials examined, several nickel-based alloys are materials that are being seriously evaluated for these high-temperature components. [25, 28]. The oxidation and other high-temperature corrosion resistances of these alloys are important because these effects can cause deterioration in the mechanical properties of superalloys through metal loss, decarburization (carbon removal), and internal oxidation.[27]. Alloy 617 is a nickel–chromium–cobalt–molybdenum alloy strengthened with solid solution and possesses an exceptional combination of high-temperature strength and oxidation resistance. [32]. For this reason, numerous studies have been conducted on the oxidation of alloys at high temperatures in air [33–36] and in various helium atmospheres to understand oxidation behavior and the stability of oxides [28, 37–40]. The corrosion damage in a simulated VHTR atmosphere has been studied by Xiao et al. [41] Bates [30], and Zheng et al. [42]. Research on short-term and long-term corrosions in high temperature helium and air was reported by Kim [27] and Jang [43]. However, the evolution of oxides and microstructural changes occurring during the high-temperature oxidation of Alloy 617 have not yet been clearly determined.

Alloy 800H is a material expected to play an important role as a structural component in fourth-generation nuclear systems. This alloy is also promising in terms of exhibiting good corrosion resistance in systems due to its high chromium (Cr) content. Incoloy 800H alloy is an austenitic, high-strength, solid solution strengthened Fe–Ni–Cr-based superalloy. Due to its high resistance to oxidation and corrosion at high temperatures, it has been selected as a potential candidate material for fourth-generation nuclear reactors [44–47]. Incoloy 800H is considered one of the candidate materials for components such as the intermediate heat exchanger, hot duct, steam generator, and fuel cladding, which are among the components of fourth-generation (Gen IV) reactors [48]. To understand the oxidation behavior of Alloy 800H and the stability of its oxides, various studies have been conducted on the oxidation of the alloy at high temperatures in air [49], in supercritical water [50, 51] and steam atmospheres [52] and some studies investigates grain boundary characters [53, 54].

Although the oxidation behaviors of 316L stainless steel, Alloy 617, and Incoloy 800H have been widely reported in the literature, most existing studies focus on these alloys individually, over limited temperature ranges, or under differing experimental conditions. A systematic and direct comparison of these three materials under identical oxidation environments and using a unified experimental methodology remains limited.

In this context, the present study provides a comprehensive and comparative investigation of the oxidation kinetics, oxide scale morphology, phase evolution, and activation energies of 316L stainless steel, Alloy 617, and Incoloy 800H in dry air over a wide temperature range (773–1473 K) relevant to VHTR applications. By combining thermogravimetric analysis (TGA), scanning electron microscopy coupled with energy-dispersive X-ray spectroscopy (SEM/EDS), and X-ray diffraction (XRD) within a single experimental framework, this work aims to establish a clear performance ranking of these alloys and to identify the key compositional and microstructural factors governing oxide scale stability.

The results of this study provide new, application-oriented insights into the relative long-term oxidation resistance of these candidate materials and offer practical guidance for material selection in very high-temperature nuclear and energy systems.

Experimental Procedures

Materials and Sample Preparation

The present study focuses on the 316L is an extra-low carbon version of Type 316 stainless steel, Ni base Alloy 617, and Incoloy alloy 800H. Table 1 shows the properties of interest for oxidation studies.

The SS-316L, Alloy 617, and Incoloy 800H strips, supplied ready-made, were cut into ideal geometries suitable for the sample basket used in the TGA device. The sample surfaces were re-sanded with 400-grit silicon carbide sandpaper to simulate the surface roughness of the actual components. Finally, the samples were cleaned with methanol and acetylene and dried in a tube furnace at 373 K for one hour. Surface preparation of the specimens was carried out using 400-grit SiC abrasive paper.

This level of surface roughness is representative of surface conditions commonly encountered in industrial applications and ensures a reproducible and comparable initial state for all specimens. Since surface roughness can influence oxidation kinetics by modifying the effective surface area as well as the initial oxide nucleation behavior, maintaining this parameter under controlled conditions is of critical importance for reliable kinetic comparisons.

Equipment and Methods

The TGA method was used to measure the oxidation rate isothermally. Subsequently, the structure of the formed oxide layer was examined using SEM (Scanning Electron Microscope) and XRD (X-ray Diffraction) techniques. The equipment used, working conditions, and methods are discussed in detail below.

Table 1 Chemical composition of SS-316L [55], alloy 617 [56] and incoloy 800H [57]

	SS-316L	Alloy 617	Incoloy 800-H
Composition (%)	Ni(12), Cr(17), Mo(2.5), Fe(65), Si(1), Mn(2), C(0.03), P(0.045), S(0.03)	Ni (54), Cr (22), Co (12.5), Mo (9), Fe (1), Ti (0.3), Mn (2), C (0.07)	Ni (30–35), Cr (19–23), Al (0.15–0.60), Fe (39.5), C (0.05–0.10),

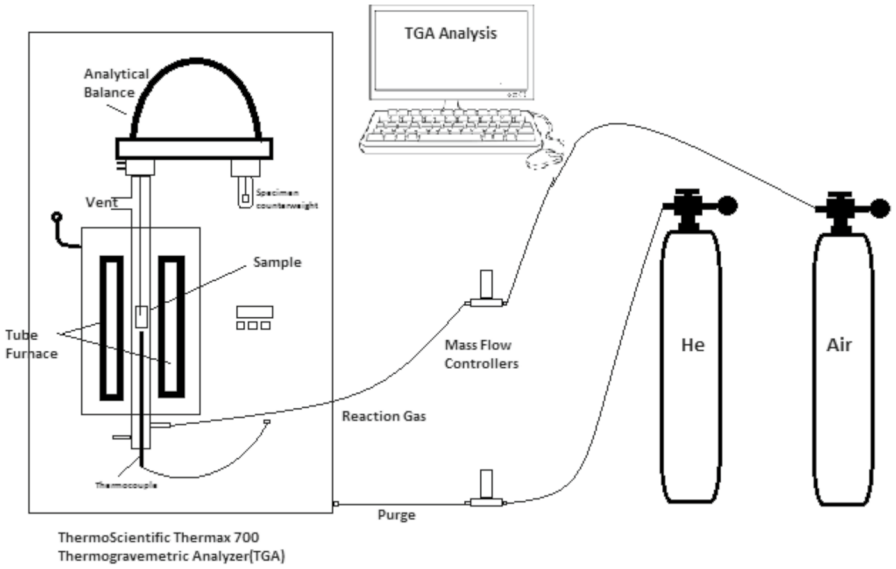

Fig. 1 A schematic of the experimental system for studying oxidation of steel

Thermogravimetric Analyzer

In the experiments, a ThermoScientific Thermax700 thermogravimetric analyzer was used to obtain mass change-temperature data in real time during the oxidation of alloys in an air atmosphere. The sample basket volume is 35 mL, the balance capacity is 100 g, and the resolution is ± 1.0 μg. In the experiments, a mixture of dry, medical-grade air and ultra-high-purity helium (He) gas was used to achieve a total flow rate of 50 mL/min. Helium was used during the heating stage to suppress premature oxidation and to avoid uncontrolled oxide formation during temperature ramp-up. Direct heating in air may lead to the development of thin and non-uniform pre-oxide films at lower temperatures, which can significantly influence early-stage oxidation kinetics. Therefore, the gas atmosphere was switched from helium to dry air only after the target temperature was reached and thermal stabilization was achieved. This procedure ensured a well-defined oxidation start point, improved reproducibility, and enabled reliable comparison of the initial oxidation behavior among different alloys. The gas flow rates were precisely adjusted using mass flow controllers. Once the desired temperature was reached, the mass change was measured under isothermal conditions. The mass change data obtained from the TGA device was transferred to a computer via automatic data acquisition software.

Figure 1 shows a schematic diagram.

Alloy samples were first heated in an ultra-high-purity helium gas environment at a constant heating rate of approximately 5 K/min until the desired oxidation temperature was reached (Fig. 2). Upon reaching the target temperature, the gas flow was switched to a 100% dry air environment. SS 316L samples were heated at temperatures of 773 K, 873 K, 973 K, 1073 K, 1173 K, and 1273 K. Alloy 617 and Incoloy 800H samples were subjected to oxidation treatment at temperatures of 1073 K, 1173 K, 1273 K, 1373 K, and 1473 K, each for a period of 24 h (24 h). To ensure the reliability of the TGA

Fig. 2 Photos of the experimental system for oxidation studies using TGA

measurements, each isothermal oxidation test was repeated least two times under identical conditions.

The applied temperature ranges were selected based on the known service temperature limits and oxidation stability of the investigated materials. 316L stainless steel is known to undergo rapid formation of Fe-rich oxides, severe scale thickening, and spallation at temperatures above approximately 1273 K, making higher-temperature oxidation tests both industrially unrealistic and kinetically less meaningful. In contrast, Alloy 617 and Incoloy 800H are candidate materials for very high temperature reactor (VHTR) applications and are designed to operate at significantly higher temperatures. Therefore, oxidation experiments for these Ni-based alloys were extended up to 1473 K to evaluate their performance under relevant extreme service conditions.

Scanning Electron Microscopy/Energy Dispersive X-Ray Spectroscopy

SEM and EDS analyses were performed using the FEI Quanta 600FEG device. The EDS detector is a Bruker Xflash 6|30 model. A backscatter electron detector (BESD) was used for all photographs with the BSED notation at the bottom of the images. In addition, to reduce charging on the sample surface, a 40 Pa low vacuum mode was applied in most of the images.

Furthermore, high-resolution images of pure samples were obtained in secondary electron mode using the Pioneer SEM/EDS device. This device has multiple scanning modes, an accelerating voltage adjustable up to 15 kV, a resolution of 512×440 pixels, a pixel size of 0.17 μm, and a magnification capacity of 1500×. Additionally, quantitative EDS data on the surface elemental composition was obtained simultaneously via the Pioneer system.

Oxide scale thickness was quantitatively measured from cross-sectional SEM images using ImageJ image analysis software. At least 10 measurements were taken at different locations for each sample to obtain average thickness values and standard deviations. Elemental distributions across the oxide scales were analyzed using EDS elemental mapping and region-based quantitative analysis. EDS elemental mapping and region-based quantitative analysis were used to support the identification of Cr-rich and Fe-rich layers.

The surface morphology and elemental composition of the oxidized samples were examined using scanning electron microscopy (SEM) combined with

energy-dispersive X-ray spectroscopy (EDS). SEM analysis was performed to investigate both surface and cross-sectional morphologies of the oxide scales formed during oxidation. EDS analysis was used to determine the elemental distribution across the oxide layers and to identify Cr-rich and Fe-rich regions.

X-Ray Diffraction

XRD (X-ray diffraction) measurements were performed using a PANalytical X'Pert Materials Research Diffractometer device with a Cu X-ray source. Analyses were performed at room temperature and a 0.4°/minute scanning speed. Measurements were taken by varying the 2θ angle in the range of 6.015°–89.985°. Copper (Cu) was used as the target, and a 1° slit was applied for both divergence and scattering.

Results and Discussions

The results and discussion section presents a comprehensive analysis of the comparative oxidation behavior of 316L stainless steel, Alloy 617, and Incoloy 800H in dry air over the temperature range of 773–1473 K. The oxidation kinetics were evaluated by TGA, while the surface and cross-sectional morphologies as well as the elemental distributions of the oxide layers were characterized using scanning electron microscopy coupled with energy-dispersive X-ray spectroscopy (SEM/EDS). In addition, phase identification and structural analysis of the formed oxides were performed by X-ray diffraction (XRD), and the corresponding activation energies for the oxidation processes were determined to elucidate the underlying kinetic mechanisms and the relative oxidation resistance of the studied alloys.

Oxidation Data from TGA

The oxidation behavior of 316L stainless steel studied by TGA in the temperature range of 773–1273 K shows two distinct trends (Fig. 3): at lower temperatures (773 K and 873 K), the samples exhibit a slight weight loss, likely due to desorption of surface species or initial reduction effects, whereas at higher temperatures (973–1273 K), there is a clear weight gain associated with oxide scale formation. The extent of oxidation increases significantly with temperature, with the most pronounced mass gain observed at 1173 K and 1273 K, indicating an acceleration of oxidation kinetics. Overall, the results confirm that the oxidation rate of 316L is strongly temperature dependent, with a transition from minor weight loss to progressive oxide growth as the temperature rises.

The Fig. 4 shows the oxidation behavior of Alloy 617 in dry air within the temperature range of 1073–1473 K, as determined by TGA. At 1073 K, the curve remains almost flat with negligible weight change, indicating that oxidation is minimal and a stable protective oxide film may form. At 1173 K, a small but steady weight gain is observed, consistent with slow, protective parabolic oxidation. As the temperature increases to 1273 K and 1373 K, the oxidation rate becomes more pronounced, with the curves showing continuous mass gain, suggesting diffusion-controlled

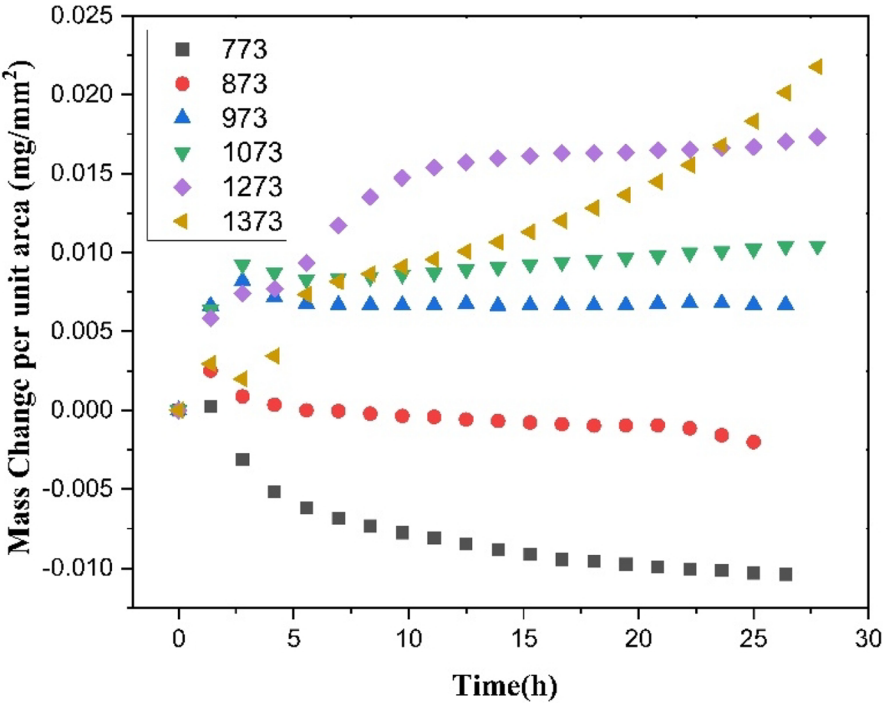

Fig. 3 Oxidation of 316L in dry-medical grade air using TGA at 773 K to 1273 K

oxide growth. At the highest temperature of 1473 K, Alloy 617 exhibits the steepest and most significant weight gain, pointing to rapid oxidation where the protective behavior of the oxide scale likely deteriorates. Overall, these results highlight the strong temperature dependence of Alloy 617's oxidation resistance, with good protective behavior at lower temperatures but increasingly aggressive oxidation and scale growth as the exposure temperature rises beyond 1273 K.

The Fig. 5 presents the oxidation behavior of Alloy 800H in dry air within the temperature range of 1073–1473 K, as measured by TGA. At lower temperatures (1073 K and 1173 K), the weight change per unit area remains minimal and progresses slowly, suggesting the development of a thin, adherent, and protective oxide layer that restricts further oxidation. As the temperature increases to 1273 K and 1373 K, the oxidation rate becomes more pronounced, with curves showing steeper slopes consistent with parabolic kinetics, indicative of diffusion-controlled oxide growth. At the highest temperature of 1473 K, the material exhibits the most significant weight gain, with the curve approaching near-linear behavior, implying a transition toward rapid and non-protective oxidation. This acceleration at elevated temperatures may be attributed to scale thickening, breakdown of protective Cr_2O_3 layers, or the formation of porous and less adherent oxides. Overall, the results highlight that Alloy 800H provides moderate oxidation resistance at intermediate temperatures but suffers from a significant loss of protective behavior as the exposure temperature rises above 1273 K.

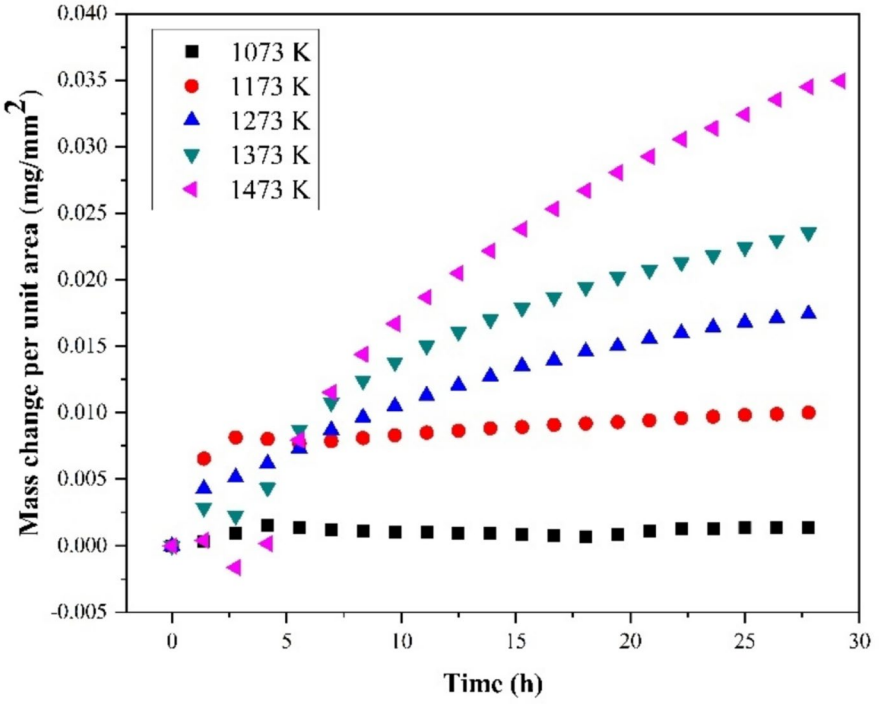

Fig. 4 Oxidation of Alloy 617 in dry-medical grade air using TGA at 1073 K to 1473 K

TGA results indicate differing oxidation behaviors for 316L, Alloy 617, and Alloy 800H in dry air. 316L shows initial weight loss at low temperatures (773–873 K) due to desorption or oxide spallation, followed by weight gain above 973 K from protective oxide formation, though spallation at 1173–1273 K suggests poor scale adherence. Alloy 617 demonstrates the best oxidation resistance, forming a stable Cr_2O_3-based layer with negligible weight change at 1073 K and maintaining low oxidation rates up to 1473 K, attributed to its high chromium and cobalt contents. Alloy 800H exhibits intermediate performance, with protective behavior up to 1173 K but accelerated oxidation and oxide breakdown above 1273 K, leading to rapid, non-protective oxidation at 1473 K.

Scanning Electron Microscopy/Energy Dispersive X-ray Spectroscopy

The SEM/EDS results obtained from the oxidized samples are presented and discussed below.

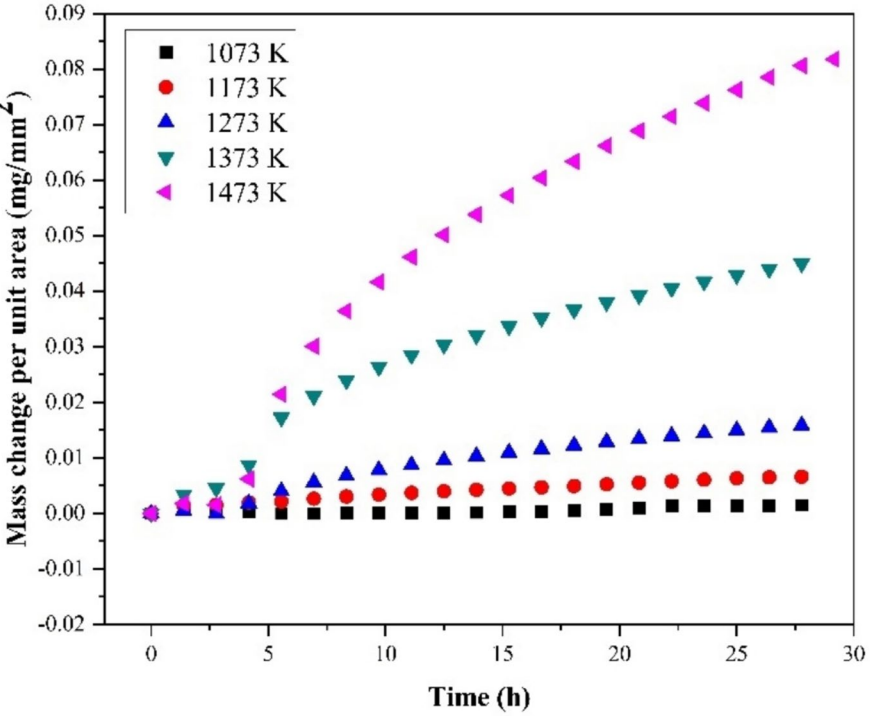

Fig. 5 Oxidation of 800H in dry-medical grade air using TGA at 1073 K to 1473 K

Surface Analysis

The SEM images of SS-316L exposed to air atmosphere at the temperatures are shown in Fig. 6. At lower temperatures (873–973 K), surface scratches from mechanical preparation remain visible, and since the oxide layer is very thin, the metallic structure of the substrate is still preserved. The surface roughness is low, with only discontinuous thin oxide films possibly present. At 1073 K, a more homogeneous and dense oxide layer develops, grain boundaries become more pronounced, and slight porosity indicates the progression of oxidation. At higher temperatures (1173 K), severe surface degradation occurs, with cracks and irregular oxide clusters forming; the oxide layer becomes non-continuous, showing spallation and detachment from the substrate, while the morphology turns rough due to accelerated oxidation and diffusion processes. At the highest temperature (1273 K), the surface is fully covered with a coarse, porous, and spalled oxide scale, with large oxide islands and separated regions, indicating a shift from parabolic to linear or even catastrophic oxidation behavior. Consequently, the protective ability of the oxide layer is lost, leading to a significant reduction in the mechanical durability of the material at elevated temperatures.

Figure 7 shows the SEM images of Alloy 617 exposed to air at different temperatures reveal a clear progression in surface morphology with increasing temperature:

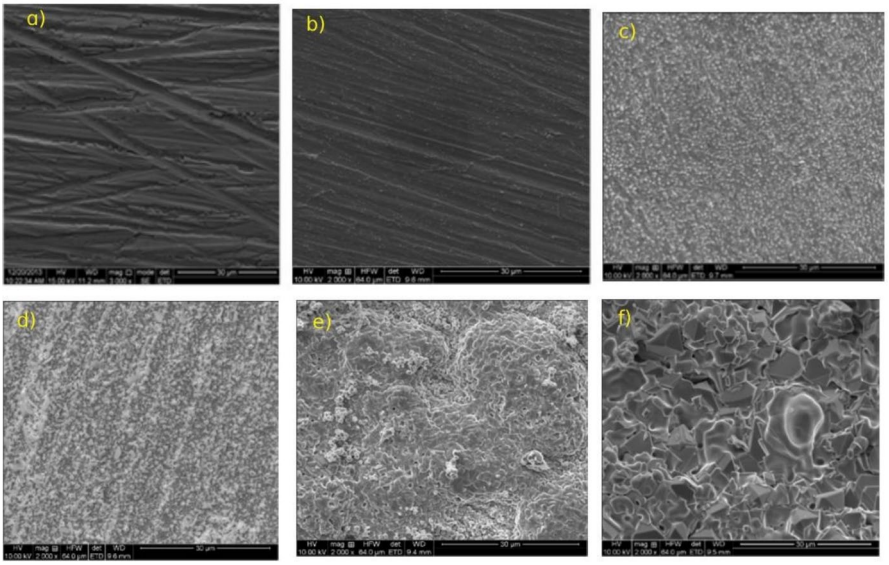

Fig. 6 The 316L SS SEM images of sample exposed to air atmosphere at the **a** 297 K temperatures **b**873 K, **c** 973 K, **d**1073 K, **e** 1173 K and **f** 1273 K, respectively

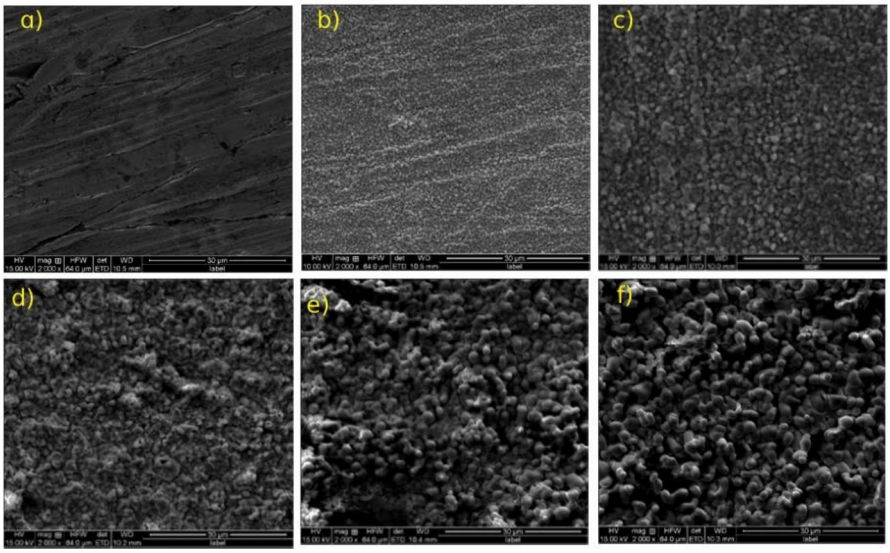

Fig. 7 The Alloy 617 SEM images of sample exposed to air atmosphere at the **a** 297 K temperatures and **b** 1073 K, **c** 1173 K, **d** 1273 K, **e** 1373 K and **f** 1473 K, respectively

at 1073 K, surface scratches from preparation are still visible and only a thin, discontinuous oxide layer is present; at 1173 K, a more homogeneous but still relatively thin oxide film forms, with slight roughening of the surface; by 1273 K, the oxide

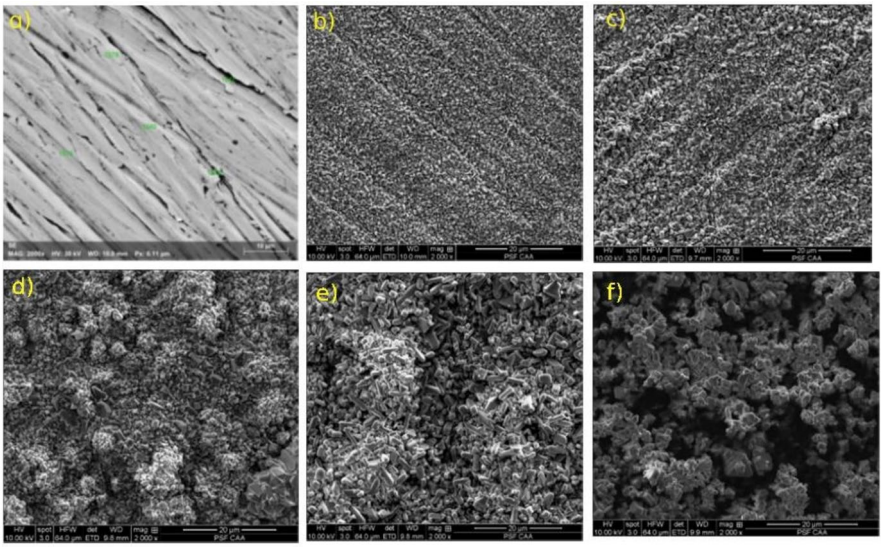

Fig. 8 The Incoloy 800-H SEM images of sample exposed to air atmosphere at the 297 K temperatures and 1073, 1173, 1273, 1373 and 1473 K, respectively

layer becomes thicker and denser, with grain boundaries more pronounced, indicating advanced oxidation; at 1373 K, the surface shows significant degradation with increased roughness, porosity, and localized cracking due to oxide spallation and loss of film uniformity; and at the highest temperature of 1473 K, the surface is completely covered by a coarse, porous, and non-protective oxide scale with large oxide islands and separation regions, reflecting catastrophic oxidation behavior and the loss of protective capability of the oxide layer.

Figure 8 display the SEM images of Incoloy 800-H exposed to air at elevated temperatures demonstrate a progressive change in surface morphology with increasing temperature. At 1073 K, surface scratches remain clearly visible, indicating that only a very thin oxide film has formed and the metallic substrate is still largely preserved. At 1173 K, a more continuous oxide layer develops, accompanied by slight surface roughening. By 1273 K, the oxide scale becomes thicker and more granular, showing a loss of surface homogeneity. At 1373 K, the surface exhibits pronounced roughness, with irregular oxide clusters, porosity, and signs of spallation, reflecting the breakdown of the protective film. At the highest temperature of 1473 K, the surface is entirely covered with a coarse, porous, and irregular oxide structure with large oxide islands, indicating catastrophic oxidation and complete loss of protective behavior.

Cross-Section Analysis

Cross-sectional SEM images of the oxide scales formed on 316L stainless steel, Alloy 617, and Incoloy 800H after exposure to air at elevated temperatures are presented in Figs. 9, 10, 11. In all cases, two distinct regions can be identified: Region

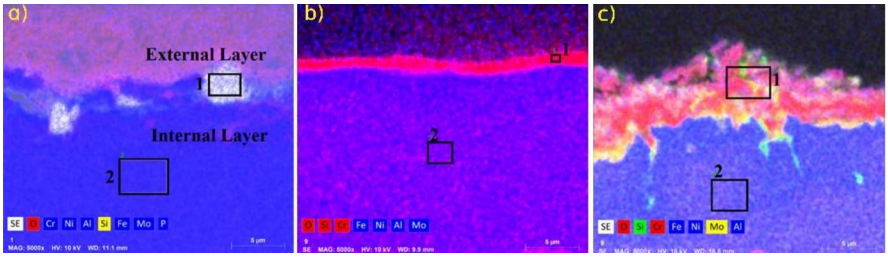

Fig. 9 The 316 SS SEM images of the cross-section of the oxide after exposure to air at **a** 773 K, **b** 1073 K and **c** 1273 K

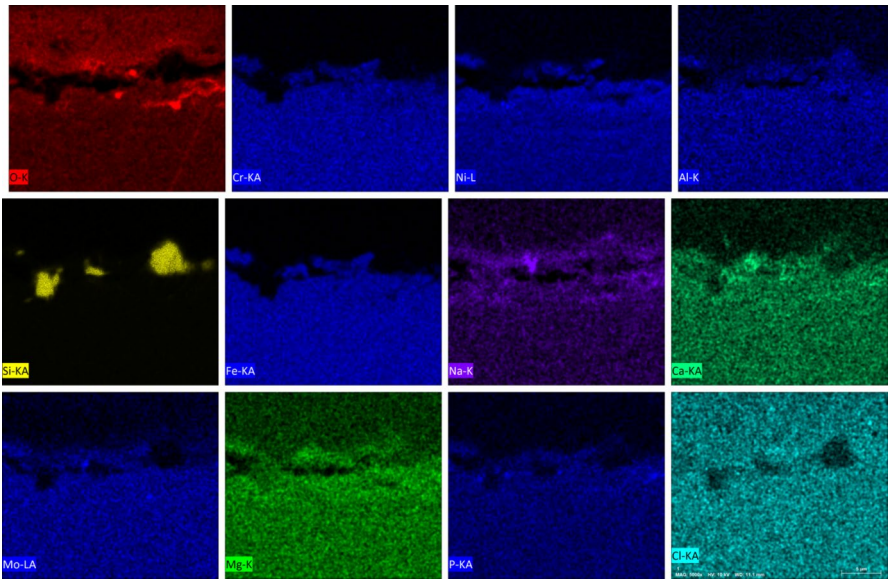

Fig. 10 The 316 SS the elemental maps in a cross-sectional area of the oxide film at 773 K

1, corresponding to the metallic substrate or the inner oxide layer adjacent to the metal, and Region 2, representing the outer oxide layer exposed to the environment.

316 SS The EDS elemental maps obtained at different temperatures reveal a progressive redistribution of alloying elements with increasing oxidation temperature. At lower temperatures, chromium is preferentially concentrated near the metal/oxide interface, indicating the formation of a chromia-based protective inner layer. With increasing temperature, iron becomes increasingly dominant throughout the oxide scale, consistent with the development of Fe-rich, non-protective oxides. These trends observed in the elemental maps (Figs. 10, 11, 12) are in good agreement with the quantitative EDS results obtained from representative regions.

The cross-sectional SEM–EDS images of 316L stainless steel exposed to air at different temperatures (Fig. 9) clearly illustrate the evolution of the oxide scale.

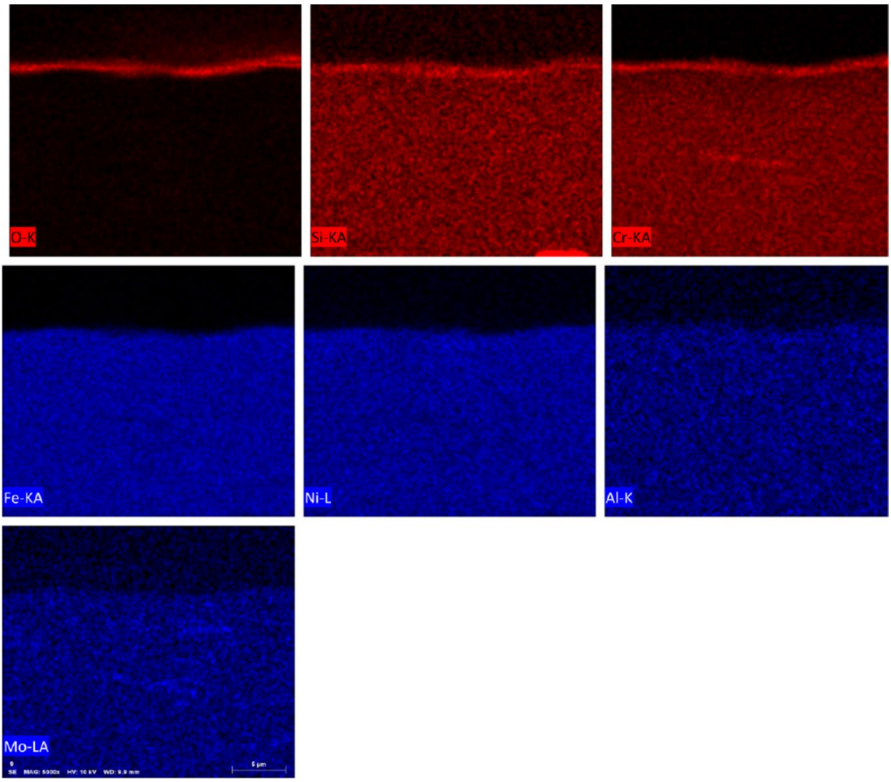

Fig. 11 The 316 SS the elemental maps in a cross-sectional area of the oxide film at 1073 K

At 773 K, a very thin, compact, and uniform oxide layer is observed, indicating limited oxidation and effective protective behavior. At 1073 K, the oxide scale thickens and develops a well-defined duplex structure consisting of a Cr-rich inner layer and a Fe-rich outer layer. The outer Fe-rich oxide is porous and poorly adherent, providing limited protection and promoting accelerated oxidation. At 1273 K, severe degradation of the oxide scale occurs; the oxide becomes significantly thicker, irregular, and porous, with pronounced spallation. EDS analysis reveals dominant iron enrichment and chromium depletion near the surface, reflecting the breakdown of chromia-based protection and the onset of catastrophic oxidation. Correspondingly, the oxide thickness increases markedly to 4.749 ± 0.967 μm (Table 2). The quantitative EDS results (mass% and atomic%) confirm Cr enrichment in the inner oxide region and Fe enrichment in the outer oxide region, supporting the SEM observations (Table 3).

Alloy 617 Alloy 617 demonstrates superior oxidation resistance over the investigated temperature range. At 1073 K, a thin, compact, and chromium-rich oxide layer forms, indicating effective protective behavior and limited oxidation. Cross-

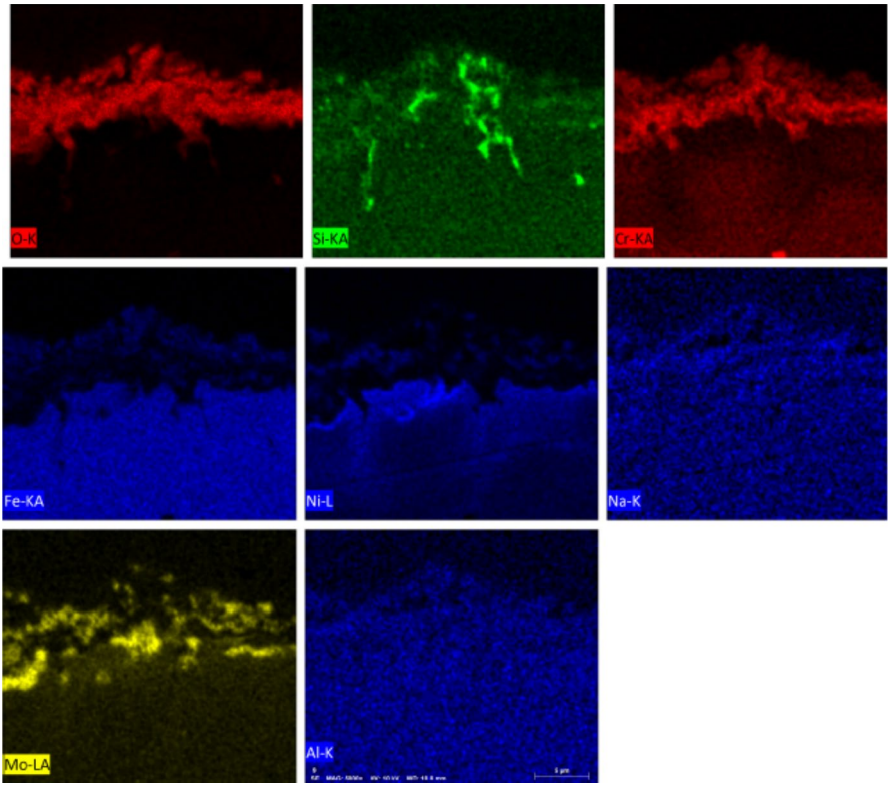

Fig. 12 The 316 SS the elemental maps in a cross-sectional area of the oxide film at 1273 K

sectional SEM–EDS images (Fig. 13) show a relatively uniform and adherent scale, consistent with the formation of a stable chromia-based protective layer.

At 1273 K, the oxide scale thickens and becomes more porous; however, the chromia-based nature of the scale is largely retained. A duplex structure is observed, consisting of an outer Cr-rich protective layer and an inner Fe-rich oxide, indicating reduced adherence and partial degradation of scale stability, yet maintaining a relatively continuous protective film.

At 1473 K, significant degradation of the oxide scale occurs. The oxide layer becomes thick, irregular, and heterogeneous, with pronounced separation between the inner and outer layers and clear evidence of spallation, reflecting the onset of catastrophic oxidation behavior (Table 4). EDS mapping (Fig. 14, 15, 16) reveals

Table 2 Oxide scale thickness of 316L stainless steel determined from cross-sectional SEM analysis

Alloy	Temperature (K)	Oxide thickness (μm)
316L	773	0.562 ± 0.127
	1073	1.166 ± 0.252
	1273	4.749 ± 0.967

Table 3 EDS elemental analysis of 316L, Region 1 and region 2 mass % and atomic %

	773 K				1073 K				1273 K			
	Region 1		Region 2		Region 1		Region 2		Region 1		Region 2	
Element	Mass (%)	Atomic (%)	Mass (%)	Atomic (%)	Mass (%)	Atomic (%)	Mass (%)	Atomic (%)	Mass (%)	Atomic (%)	Mass (%)	Atomic (%)
Oxygen	1.42	4.51	1.05	4.15	16.89	66.25	0.84	3.14	26.78	61.63	0.67	2.64
Aluminum	0.18	0.34	0.05	0.12	0.22	0.52	0.33	0.06	0	0	0.04	0.09
Silicon	51.18	92.61	0.61	1.38	0.68	1.51	0.37	0.78	2.43	3.19	0.6	1.36
Chromium	0.89	0.87	14.32	17.41	23.22	28.03	16.67	19.06	29.31	20.76	12.74	15.47
Iron	0.57	0.52	57.79	67.91	2.92	3.29	63.48	67.58	16.68	11	59.45	67.2
Nickel	0.08	0.07	9.51	10.24	0	0	7.94	8.04	2.97	1.87	11.25	12.1
Molybde-num	0.47	0.25	1.61	1.06	0.62	0.41	2.18	1.35	4.03	1.55	1.73	1.14

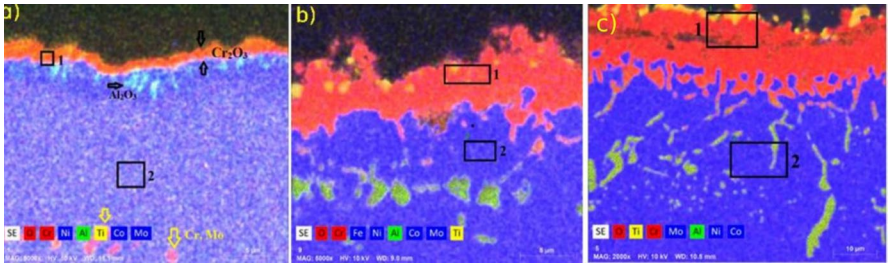

Fig. 13 The 617 SEM images of the cross-section of the oxide after exposure to air at **a** 1073 K, **b** 1273 K and **c** 1473 K

increased elemental heterogeneity and pronounced iron enrichment at this temperature, indicating partial loss of chromia-based protection. Nevertheless, the measured oxide thickness remains lower than that of Incoloy 800H under similar conditions, highlighting the comparatively superior high-temperature stability of Alloy 617.

Quantitative oxide thickness measurements obtained from cross-sectional SEM analysis (Table 5) further support these observations, showing a progressive increase in scale thickness from 1.020 ± 0.338 µm at 1073 K to 6.012 ± 0.263 µm at 1473 K (Table 5).

Quantitative EDS results for Alloy 617 (Table 4) reveal a clear compositional differentiation between the inner (Region 1) and outer (Region 2) oxide layers at all investigated temperatures. At 773 K and 1073 K, chromium is the dominant element in the inner oxide region, confirming the formation of a chromia-based protective layer adjacent to the metal surface. In contrast, the outer oxide region is enriched in nickel and cobalt, indicating outward diffusion of these elements during oxidation. At 1273 K, although chromium remains a major constituent of the inner oxide layer, a noticeable increase in iron and nickel content is observed in the outer region, reflecting increased elemental redistribution and partial degradation of scale stability. These compositional trends are consistent with the SEM observations and EDS mapping results, supporting the conclusion that Alloy 617 maintains chromia-based protection up to intermediate temperatures, with partial loss of protectiveness at higher temperatures.

Incoloy 800H Cross-sectional SEM images of the oxide scales formed on Incoloy 800H after exposure to air at 1073 K, 1273 K, and 1473 K are shown in Fig. 17. Similar to the other investigated alloys, two distinct regions are observed: an inner oxide layer adjacent to the metal substrate (Region 1) and an outer oxide layer exposed to the environment (Region 2).

At 1073 K, Incoloy 800H forms a thin, compact, and relatively uniform oxide layer, indicating effective initial protection against oxidation. Quantitative EDS analysis (Table 6) reveals chromium enrichment within the oxide scale, confirming the formation of a chromia-based protective layer. Elemental maps at this temperature (Fig. 18) further show a relatively homogeneous distribution of chromium, consistent with stable oxide growth and limited elemental redistribution.

Table 4 EDS elemental analysis of alloy 617, Region 1 and region 2 mass % and atomic %

	773 K				1073 K				1273 K			
	Region 1		Region 2		Region 1		Region 2		Region 1		Region 2	
Element	Mass (%)	Atomic (%)	Mass (%)	Atomic (%)	Mass (%)	Atomic (%)	Mass (%)	Atomic (%)	Mass (%)	Atomic (%)	Mass (%)	Atomic (%)
Oxygen	22.46	57.11	0.53	2.37	24.23	64.18	0.67	3.44	16.78	57.82	3.45	15.61
Aluminum	0.47	0.7	0.64	1.71	0.35	0.55	0.17	0.51	0.03	0.07	1.03	2.75
Silicon	0.12	0.17	0.14	0.34	0	0	0.09	0.26	0.23	0.45	0	0
Titanium	1.3	1.11	0.42	0.63	2.38	2.1	0.3	0.51	3.02	3.48	0	0
Chromium	46.85	36.66	21.58	29.68	39	31.78	14.82	23.43	35.51	37.65	15.08	20.99
Cobalt	0.98	0.68	5.95	7.22	0.3	0.22	6.27	8.75	0.27	0.25	6.47	7.94
Nickel	4.11	2.85	43.2	52.64	0.91	0.66	39.1	54.75	0.16	0.15	37.67	46.45
Molybdenum	1.71	0.73	7.27	5.42	0.18	0.08	8.88	7.61	0.22	0.13	8.3	6.26

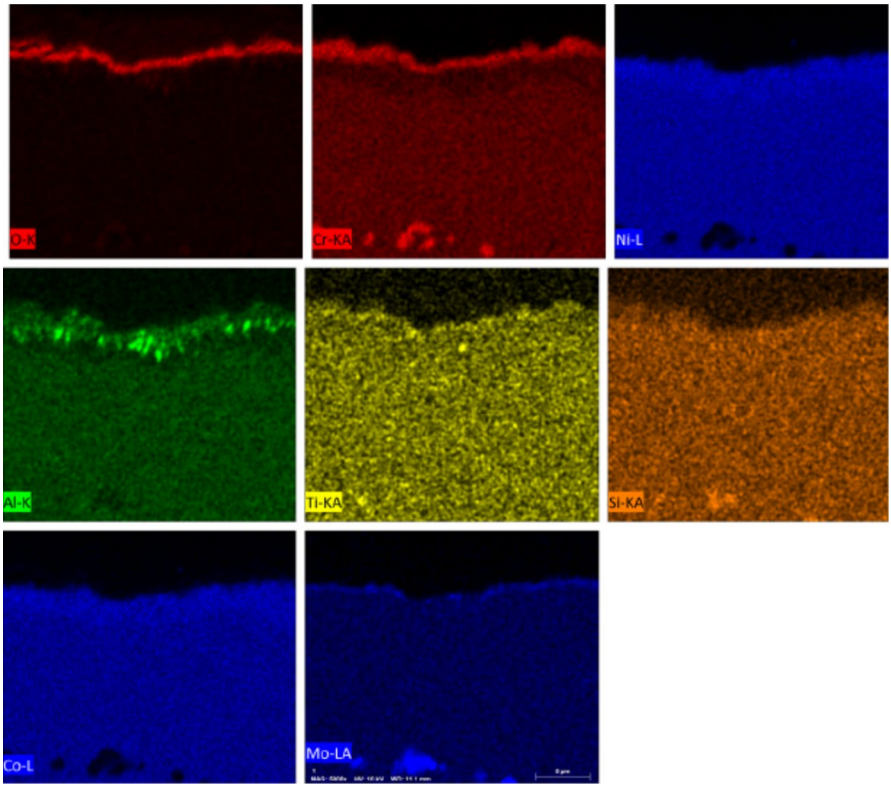

Fig. 14 The 617 alloy the elemental maps in a cross sectional area of the oxide film at 1073 K

At 1273 K, the oxide scale thickens significantly and develops a clear duplex structure. Cross-sectional SEM–EDS images (Fig. 17b) reveal increased porosity and reduced adherence of the oxide layer. EDS results indicate continued chromium enrichment within the oxide, accompanied by increased iron content, suggesting partial degradation of the chromia-based protective layer. Elemental mapping (Fig. 19) confirms enhanced elemental redistribution, with chromium still present but less uniformly distributed across the scale.

At 1473 K, extensive oxidation damage is observed. The oxide scale becomes highly irregular, porous, and heterogeneous, with pronounced separation between the inner and outer layers and clear evidence of spallation (Fig. 17c). Elemental maps (Fig. 20) show significant iron enrichment throughout the oxide scale, indicating the breakdown of chromia-based protection and the formation of Fe-rich, non-protective oxides. Although the measured oxide thickness at this temperature (10.15 ± 0.356 µm, Table 7) primarily corresponds to the inner compact layer, the outer porous oxide layer is partially spalled and therefore not fully captured in the thickness measurement. Nevertheless, the extensive porosity and spallation clearly indicate catastrophic oxidation behavior.

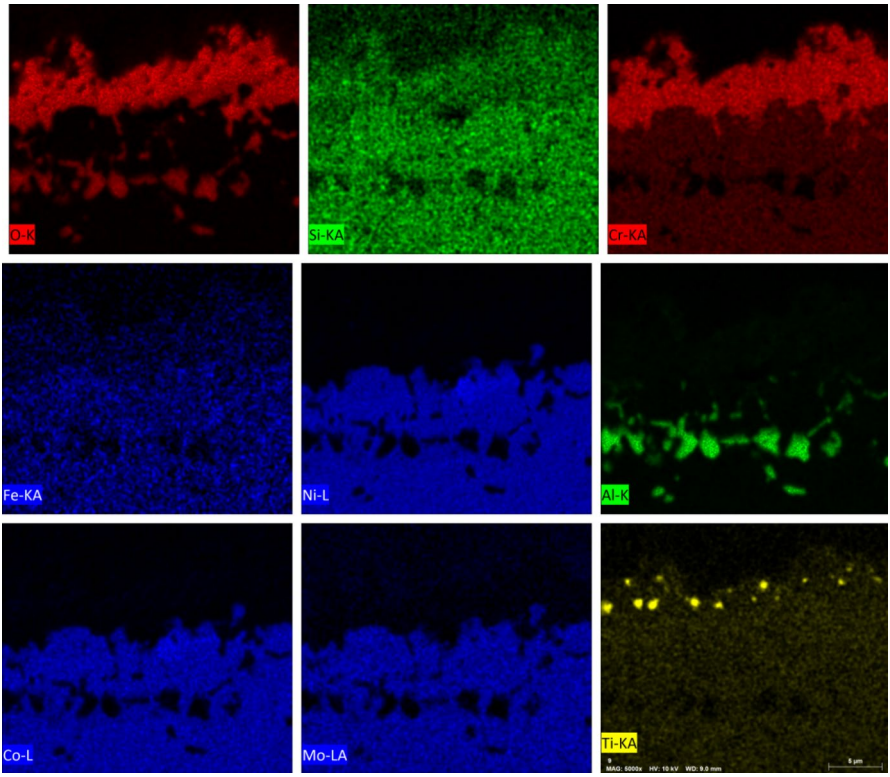

Fig. 15 The 617 alloy the elemental maps in a cross-sectional area of the oxide film at 1273 K

The quantitative oxide thickness measurements (Table 7) demonstrate a strong dependence on temperature, with a rapid increase in scale thickness above 1273 K. Compared to Alloy 617, which maintains a relatively thin and compact oxide scale even at 1473 K, Incoloy 800H exhibits significantly thicker and less stable oxide scales at elevated temperatures. In contrast, 316L stainless steel forms even thicker and more poorly adherent Fe-rich oxide scales, reflecting inferior oxidation resistance.

The comparative SEM–EDS analyses of 316L, Alloy 617, and Alloy 800H reveal significant differences in their high-temperature oxidation behavior. For 316L, the oxide scale develops as a duplex structure with a Cr-rich outer layer and a Fe-rich inner layer, but at elevated temperatures it becomes porous, irregular, and prone to spallation, reflecting poor scale adherence and limited protective capability. Alloy 617 exhibits the most stable performance, forming a thin and uniform Cr-rich protective layer at 1073 K and maintaining partial integrity even at 1273 K, although some porosity and thickening are observed; only at 1473 K does the oxide scale show extensive degradation with spallation. Alloy 800H demonstrates intermediate behavior: while initially forming a compact protective layer similar to Alloy 617, it shows earlier breakdown at 1273 K with increasing porosity and structural

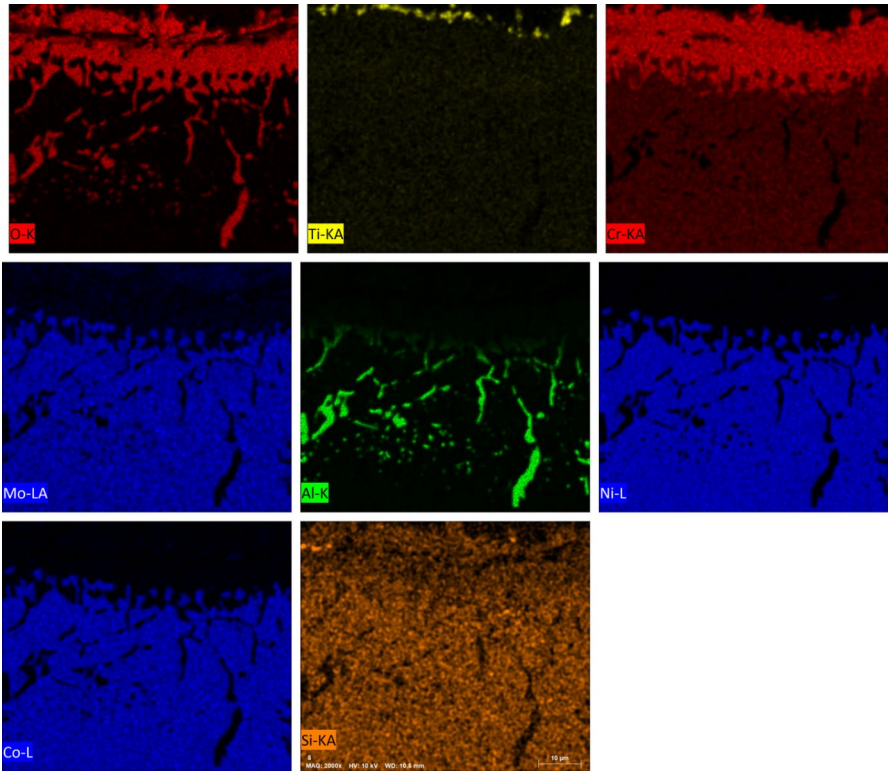

Fig. 16 The 617 alloy the elemental maps in a cross-sectional area of the oxide film at 1473 K

Table 5 Oxide scale thickness of alloy 617 determined from cross-sectional SEM analysis

Alloy	Temperature (K)	Oxide thickness (μm)
617	1073	1.020 ± 0.338
	1273	4.110 ± 0.650
	1473	6.012 ± 0.263

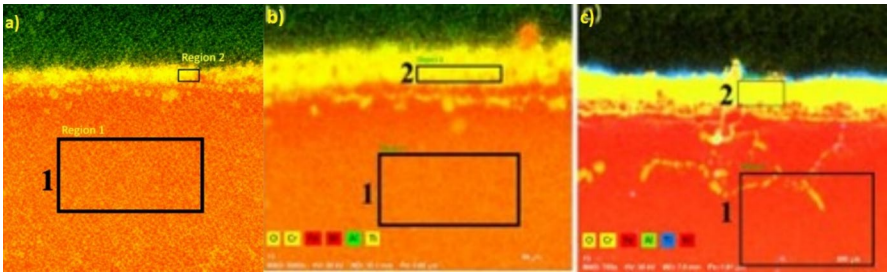

Fig. 17 The 800H SEM images of the cross-section of the oxide after exposure to air at **a** 1073 K, **b** 1273 K and **c** 1473 K

Table 6 EDS elemental analysis of 800H, Region 1 and region 2 mass % and atomic %

	773 K				1073 K				1273 K			
	Region 1		Region 2		Region 1		Region 2		Region 1		Region 2	
Element	Mass (%)	Atomic (%)	Mass (%)	Atomic (%)	Mass (%)	Atomic (%)	Mass (%)	Atomic (%)	Mass (%)	Atomic (%)	Mass (%)	Atomic (%)
Carbon	13.39	41.19	26.83	49.03	9.93	33.37	19.31	40.65	11.09	35.96	9.25	20.96
Oxygen	0.59	1.35	21.96	30.14	0.48	1.22	18.88	29.84	0.91	2.23	26.85	45.68
Aluminum	0.25	0.34	0	0	0.29	0.44	0.17	0.16	0.45	0.65	0.05	0.05
Silicon	0.26	0.34	0.08	0.06	0.32	0.47	0.45	0.4	0.23	0.31	0.14	0.13
Chlorine	0.04	0.05	0.3	0.19	0.04	0.04	0.1	0.07	0.03	0.03	0.05	0.04
Titanium	0.32	0.24	0.68	0.31	0.32	0.27	1.01	0.54	0.11	0.09	0.41	0.23
Chromium	19.44	13.81	22.94	9.68	19.8	15.37	38.6	18.78	16.32	12.22	58.28	30.51
Iron	40.64	26.89	21.43	8.43	42.33	30.6	14.01	6.34	44.04	30.71	3.61	1.76
Nickel	25.07	15.78	5.78	2.16	26.49	18.22	7.46	3.21	26.82	17.79	1.36	0.63

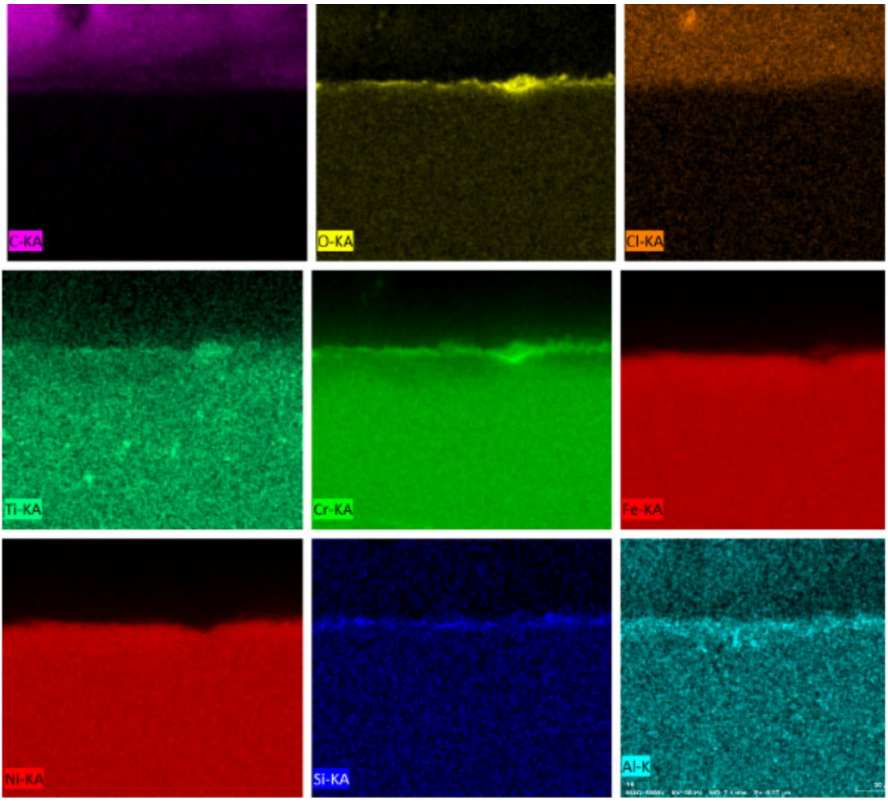

Fig. 18 The 800H alloy the elemental maps in a cross sectional area of the oxide film at 1073 K

heterogeneity, and at 1473 K the protective film deteriorates severely, leading to extensive spallation.

Characterization of the Oxidized Layer with X-Ray Diffraction

Figure 21, the XRD patterns of 316L stainless steel illustrate the progressive formation and transformation of oxide phases with increasing temperature. The pure sample exhibits only the γ-austenitic matrix peaks, confirming its single-phase structure. At 773 K, the first oxide phases, primarily Cr–Fe–Ni spinels, begin to appear, forming a thin and continuous protective layer. Between 873 and 973 K, additional phases such as Fe_2O_3 (β) and Cr_2FeO_4 (ε) emerge with higher intensities, indicating the growth of a more complex and thicker oxide scale. At 1073–1173 K, Fe-rich oxides (hematite and magnetite) become more dominant while spinel phases remain present, reflecting the development of a multi-layered oxide structure. At 1273 K, Fe-oxide peaks intensify significantly whereas the protective Cr-rich phases decrease, demonstrating a breakdown of the chromia-based protective scale and the

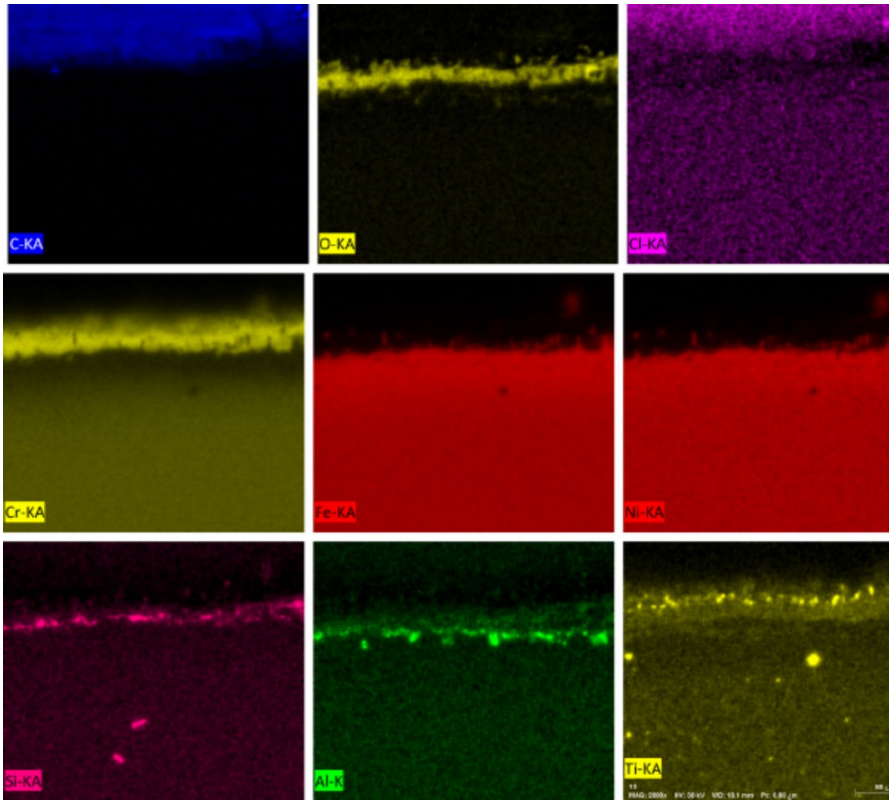

Fig. 19 The 800H alloy the elemental maps in a cross-sectional area of the oxide film at 1273 K

predominance of iron oxides, which signals reduced oxidation resistance and the onset of accelerated oxidation.

Figure 22, the XRD patterns of Alloy 617 reveal the progressive formation and evolution of oxide phases with increasing temperature. The pure sample exhibits only the γ-austenitic matrix peaks, confirming its single-phase structure prior to oxidation. At 1073 K, distinct peaks of Cr_2O_3 (ψ) and Cr–Fe–Ni spinel oxides (φ) appear, indicating the initial development of a protective chromia-based layer. With further exposure at 1173–1273 K, the intensity of Cr_2O_3 peaks increases and spinel phases become more pronounced, reflecting the growth of a thicker and more stable protective scale. At 1373 K, both Cr_2O_3 and spinel oxides are strongly present, producing a more complex oxide structure. At the highest temperature of 1473 K, Cr_2O_3 remains dominant but spinel oxides intensify significantly, leading to a thicker, heterogeneous scale that, while still partly protective, suggests a reduction in homogeneity and long-term stability of the oxide film. Although Cr_2O_3 peaks are still detected by XRD at 1473 K, its presence does not necessarily indicate a fully protective oxide scale. At such high temperatures, chromia is known to suffer from chromium volatilization and thermodynamic instability, leading to chromium

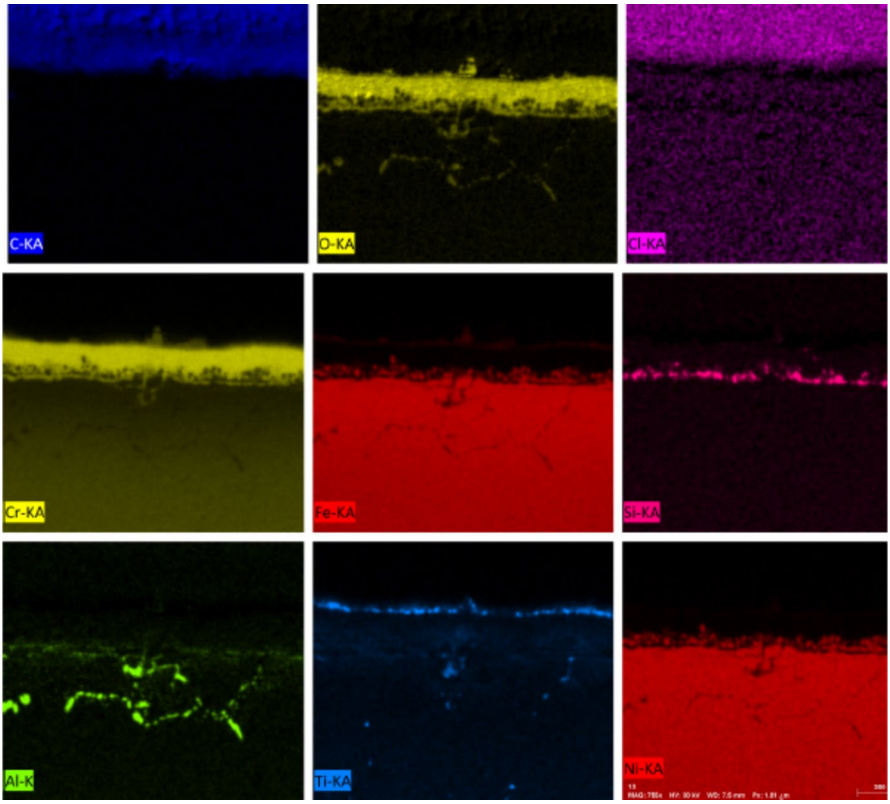

Fig. 20 The 800H alloy the elemental maps in a cross sectional area of the oxide film at 1473 K

Table 7 Oxide scale thickness of 800H determined from cross-sectional SEM analysis

Alloy	Temperature (K)	Oxide thickness (μm)
800H	1073	0.85 ± 0.232
	1273	6.750 ± 0.347
	1473	10.15 ± 0.356

depletion at the metal/oxide interface and progressive degradation of scale integrity. This degradation is consistent with the porous and heterogeneous oxide morphologies observed in cross-sectional SEM images at 1473 K.

Figure 23, the XRD patterns of Incoloy 800H reveal a clear evolution of oxide phases with increasing temperature. The pure sample shows only the characteristic peaks of the γ-austenitic matrix, indicating a single-phase structure. After exposure at 1073–1173 K, diffraction peaks corresponding to Cr_2O_3 and spinel-type oxides such as $(Ni,Fe)(Cr,Fe)_2O_4$ appear, suggesting the initial formation of a protective oxide film. Spinel-type oxides play a dual role during oxidation. At intermediate temperatures, these phases can contribute to improved scale adhesion by

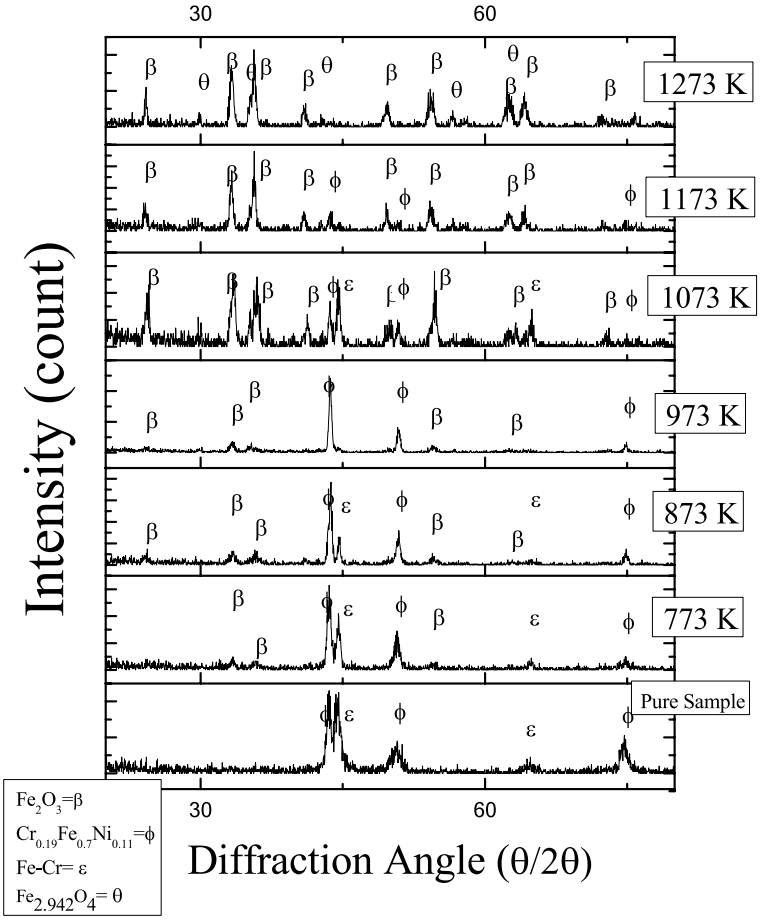

Fig. 21 X-Ray diffraction of 316L Stainless Steel pure sample and 773 K to 1273 K samples

accommodating cation diffusion and reducing growth stresses. However, at higher temperatures, increasing Fe enrichment in spinel phases promotes the formation of porous, fast-growing oxides, which deteriorate scale adherence and accelerate oxidation. At 1273–1373 K, the intensities of Fe-rich oxides, including Fe_2O_3 and Fe_3O_4, become more pronounced while spinel phases are further developed, reflecting a thickening and less protective scale. At 1473 K, Fe-oxides dominate the diffraction pattern and Cr_2O_3 peaks are significantly reduced, indicating the breakdown of the protective chromia layer and the transition to non-protective, iron-rich oxides, which is consistent with catastrophic oxidation behavior at high temperature.

The XRD analyses of 316L, Alloy 617, and Alloy 800H confirm clear differences in their oxide phase evolution with increasing temperature. For 316L, oxidation is dominated by Fe-rich oxides such as Fe_2O_3 and Fe_3O_4 along with spinel

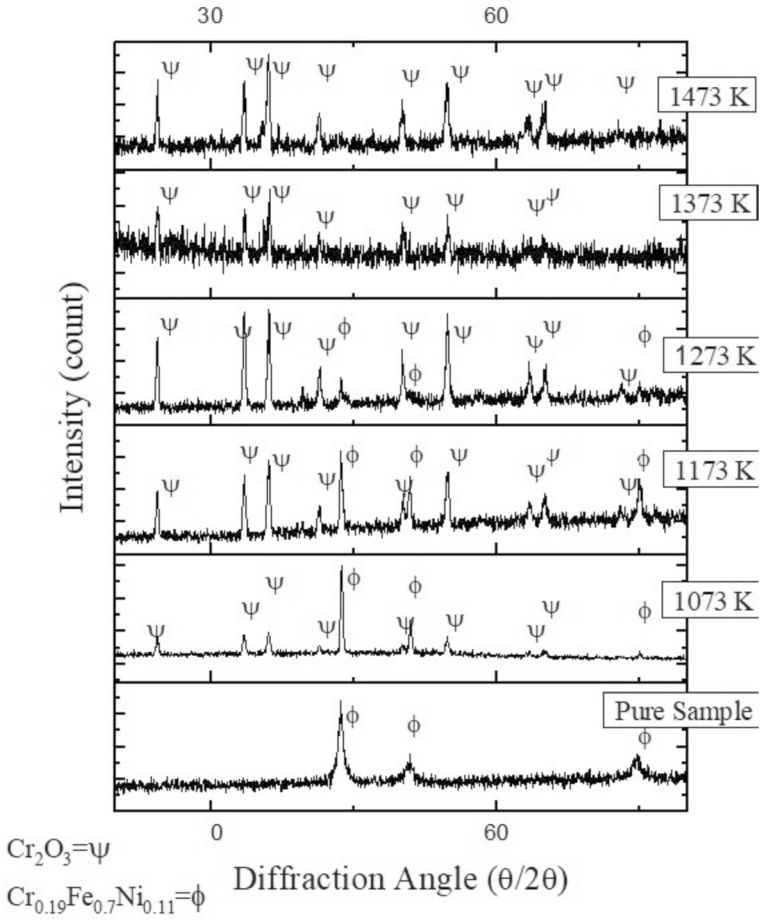

Fig. 22 X-Ray diffraction of Alloy 617 pure sample and 1073 K to 1473 K samples

phases, indicating selective Fe oxidation and the breakdown of protective chromia, which explains its poor high-temperature resistance and tendency toward spallation. Alloy 800H exhibits both Cr_2O_3 and Fe-rich oxides, showing moderate protection at lower temperatures but with a gradual shift toward Fe oxides at 1273–1473 K, reflecting the reduced stability of chromia and the formation of more porous scales. In contrast, Alloy 617 maintains Cr_2O_3 as the dominant phase across the full temperature range, with only minor contributions from spinels and Ni-based oxides, highlighting its ability to form a continuous and adherent chromia layer that provides the most effective long-term oxidation resistance.

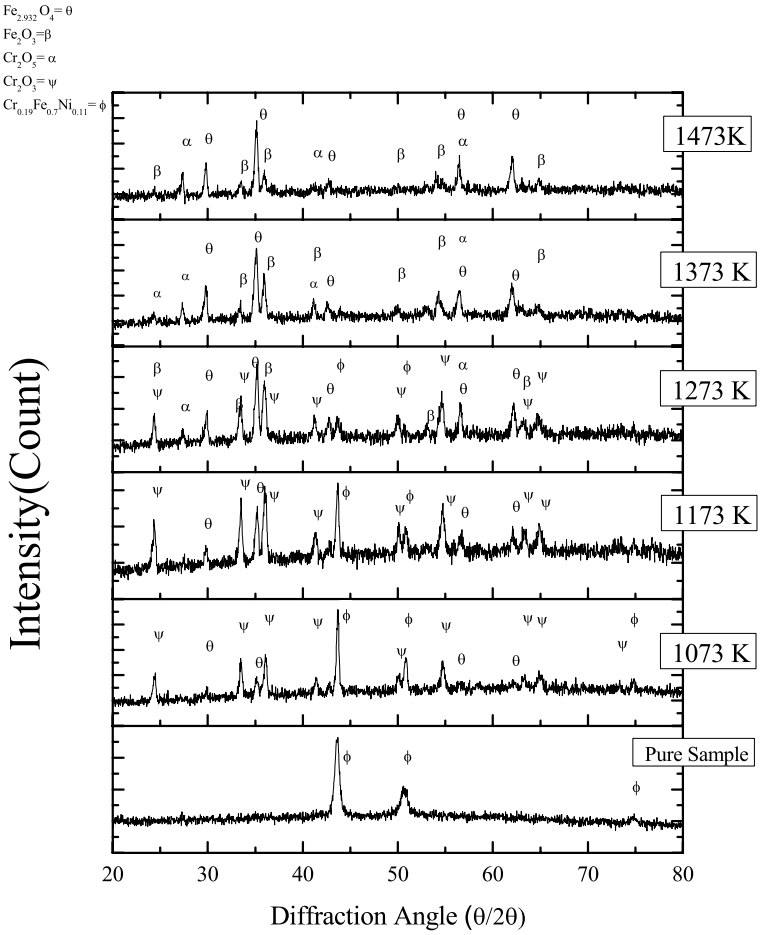

Fig. 23 X-Ray diffraction of Incoloy 800H alloy pure sample and 1073 K to 1473 K samples

Overall, the combined XRD, SEM, and TGA results indicate distinct oxidation mechanisms for the sturatdied alloys. 316L stainless steel is dominated by Fe-rich oxides and spinels, leading to poor scale adhesion and rapid oxidation. In Incoloy 800H, chromia-based protection is partially effective at intermediate temperatures but degrades significantly at 1273–1473 K due to chromium depletion and spinel formation. In contrast, Alloy 617 maintains a chromia-dominated scale over a wider temperature range, delaying the onset of catastrophic oxidation despite partial chromia degradation at 1473 K.

Parabolic Rate Constants (k_p), Kinetic Analysis, and Activation Energy

The temperature dependence of the parabolic oxidation rate constant k_p follows the Arrhenius-type relationship [58]:

Table 8 Parabolic oxidation rate constants (k_p) of the investigated alloys at different temperatures

Sıcaklık (K)	SS-316L (k_p)	Alloy 617 (k_p)	Incoloy 800H (k_p)
873	6.76×10^{-9}	–	–
973	2.58×10^{-5}	–	–
1073	1.79×10^{-6}	1.78×10^{-8}	7.95×10^{-8}
1173	9.53×10^{-6}	1.80×10^{-6}	1.69×10^{-6}
1273	1.51×10^{-5}	1.14×10^{-5}	1.03×10^{-5}
1373	–	2.19×10^{-5}	7.95×10^{-5}
1473	–	4.86×10^{-5}	2.62×10^{-4}

$$k_p = A\exp\left(\frac{-Q}{RT}\right)$$

where A is the pre-exponential factor and Q is the apparent activation energy of the parabolic oxidation process. Taking the natural logarithm of both sides gives:

$$\ln(k_p) = \ln(A) - \frac{Q}{R}\left(\frac{1}{T}\right)$$

Accordingly, a plot of $\ln(k_p)$ versus $1/T$ yields a straight line, the slope of which is equal to $-Q/R$. The activation energy can therefore be calculated from the slope using:

$$Q = -(slope) \times R$$

where R is the universal gas constant(8.31 J/mol K).

In this study, the parabolic rate constants k_p were obtained from the slopes of the $(\Delta m/\mathrm{A})^2$ versus time curves in the parabolic regime, and the corresponding Arrhenius plots of $\ln(k_p)$ versus $1/T$ were used to determine the

Table 8 Parabolic oxidation rate constants (k_p) of SS-316L, Alloy 617, and Incoloy 800H alloys determined from the slopes of the $(\Delta\mathrm{m/A})^2$ versus time curves in the parabolic regime. The calculated parabolic rate constants (k_p) at each temperature are summarized in Table 8. These values confirm that the oxidation process is predominantly diffusion-controlled within the investigated temperature range.

As illustrated in Fig. 24, the parabolic rate constants (k_p) increase significantly with temperature for all investigated alloys, reflecting the thermally activated nature of the oxidation process. Among the materials, Alloy 617 exhibits the lowest k_p values, indicating superior oxidation resistance.

Figure 25 presents the combined Arrhenius plots of the parabolic oxidation rate constants (k_p) for 316L stainless steel, Alloy 617, and Incoloy 800H. For all investigated alloys, a clear linear relationship between $\ln(k_p)$ and 1/T is observed, confirming that the oxidation kinetics follow the classical Arrhenius behavior. The negative slopes of the fitted lines indicate that the oxidation rate constants

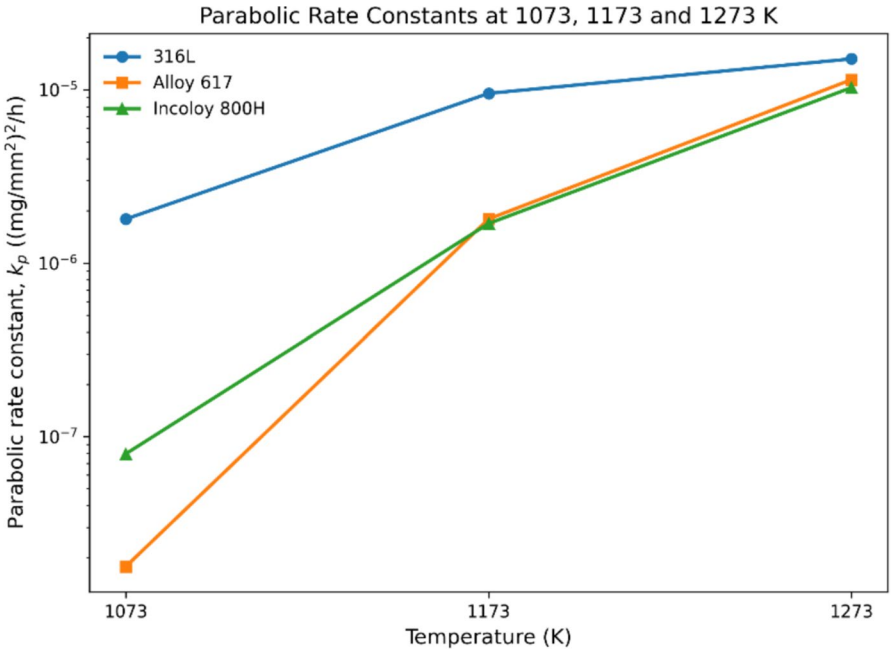

Fig. 24 Temperature dependence of the parabolic oxidation rate constants (k_p) of 316L stainless steel, Alloy 617, and Incoloy 800H at 1073, 1173, and 1273 K

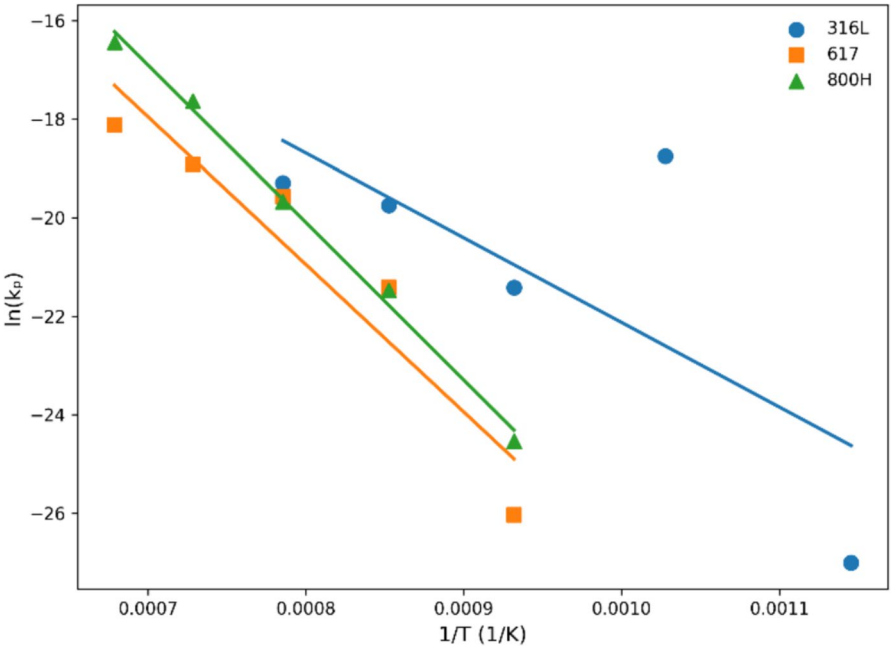

Fig. 25 Arrhenius plot and exhibited activation energy for the SS-316L(873 K to 1273 K), alloy 617 and incoloy 800H (1073 K to 1473 K)

increase with increasing temperature, reflecting the thermally activated nature of the oxidation processes.

The calculated activation energies were determined as 142.99 kJ mol^{-1} for 316L, 249.04 kJ mol^{-1} for Alloy 617, and 265.83 kJ mol^{-1} for Incoloy 800H. The relatively low activation energy of 316L suggests a less effective diffusion barrier, which is consistent with the formation of non-protective, Fe-rich oxide scales at elevated temperatures. In contrast, Alloy 617 and Incoloy 800H exhibit significantly higher activation energies, indicating the formation of more stable and diffusion-resistant oxide layers.

Although Incoloy 800H shows the highest apparent activation energy, its long-term oxidation resistance is limited by the degradation of the Cr_2O_3-based protective scale at temperatures above 1273 K. Alloy 617, despite having a slightly lower activation energy, maintains a more continuous, adherent, and stable chromia-based oxide layer over a wider temperature range. Therefore, the superior oxidation resistance of Alloy 617 arises not only from kinetic factors but also from the morphological stability and integrity of its oxide scale.

Figure 26 shows the combined Arrhenius plots of $\ln(k_p)$ versus 1/T for 316L, Alloy 617, and Incoloy 800H at 1073 K, 1173 K, and 1273 K. A linear relationship is observed for all alloys, confirming Arrhenius-type behavior. The calculated activation energies (Table 8) are 122.52 kJ·mol^{-1} for 316L, 370.7 kJ·mol^{-1} for Alloy 617, and 277.45 kJ·mol^{-1} for Incoloy 800H. The high activation energy of Alloy 617 indicates superior resistance to oxidation, while 316L exhibits the lowest resistance.

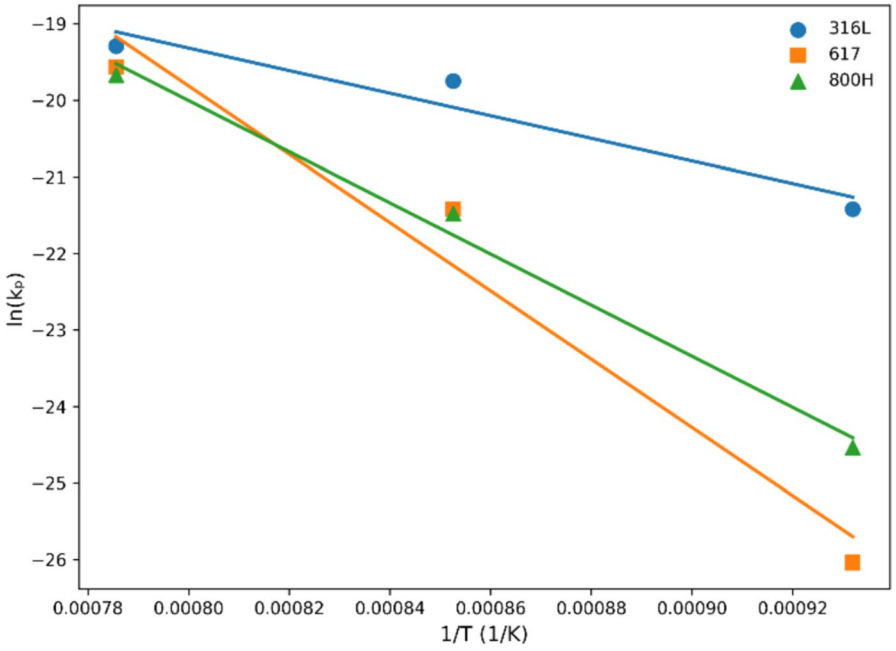

Fig. 26 Arrhenius plot and exhibited activation energy for the SS-316L, alloy 617 and incoloy 800H (1073 K to 1273 K)

The resolution of the balance used in TGA measurements is ± 1 μg, and the experimental uncertainty in mass change has been evaluated taking this value into account. Systematic uncertainty sources (gas flow stability, temperature fluctuations, and surface preparation differences) have been considered for each measurement. The effect of these uncertainties on *k*p and activation energy calculations has been evaluated during regression analysis.

The relatively high activation energy obtained for Incoloy 800H indicates that its oxidation process is strongly temperature dependent and that diffusion through the oxide scale is kinetically hindered within the investigated temperature range. The high degree of linear correlation ($R^2 \approx 0.99$) confirms that the experimental data are well described by the Arrhenius relationship, demonstrating that oxidation is thermally activated and diffusion controlled under these conditions. The elevated activation energy suggests the formation of a dense and initially protective oxide layer, primarily composed of Cr_2O_3 with contributions from Al_2O_3, which effectively restricts ionic transport through the scale.

However, a high activation energy alone does not necessarily imply superior long-term oxidation resistance. Oxidation resistance must also be assessed in terms of oxide scale continuity, adhesion, morphological stability, and resistance to porosity and spallation. At low and intermediate temperatures, oxidation kinetics predominantly follow parabolic behavior, indicating diffusion-controlled oxide growth. At higher temperatures, particularly in the range of 1373–1473 K, significant deviations from parabolic kinetics are observed in some alloys. These deviations are associated with oxide scale thickening, increased porosity, crack formation, and spallation, indicating that oxidation cannot be described by a single kinetic mechanism over the entire temperature range.

Although Incoloy 800H exhibits the highest apparent activation energy among the investigated alloys, SEM–EDS and XRD analyses reveal that its Cr_2O_3-based protective layer becomes unstable above 1273 K. At these temperatures, Fe-rich oxides increasingly dominate the scale, leading to the formation of porous and poorly adherent oxide layers that compromise protective performance and result in accelerated oxidation.

In contrast, Alloy 617 forms a more stable, continuous, and adherent Cr_2O_3-dominated oxide scale over a wider temperature range. Despite having a slightly lower activation energy than Incoloy 800H, the superior morphological stability and scale integrity of Alloy 617 provide more effective long-term protection under extreme high-temperature conditions. Consequently, oxidation resistance in this study is evaluated not solely on the basis of kinetic parameters, but through a combined consideration of activation energy, oxide scale morphology, microstructural stability, and adhesion.

For Alloy 617, oxidation behavior remains predominantly parabolic over a broad temperature range; however, deviations from ideal parabolic kinetics become more pronounced at 1473 K. Thermogravimetric analysis shows an initial transient followed by accelerated mass gain, suggesting partial loss of scale protectiveness at this temperature. This behavior is likely associated with scale damage, increased porosity, and changes in the rate-controlling mechanism. Accordingly, the parabolic

rate constant (k_p) at 1473 K was determined from the time interval in which parabolic behavior remained dominant ($t \geq 5.56$ h).

The observed increase in parabolic rate constants at elevated temperatures correlates closely with the increasing presence of Fe-rich spinel and iron oxide phases identified by XRD. These phases promote the formation of porous, rapidly growing oxide scales, leading to deviations from ideal diffusion-controlled parabolic kinetics. This kinetic transition is fully consistent with the microstructural evolution observed in cross-sectional SEM analyses.

Conclusions

This study provides a systematic and direct comparison of the high-temperature oxidation behavior of 316L stainless steel, Incoloy 800H, and Alloy 617 under identical dry air conditions over a wide temperature range relevant to very high temperature reactor (VHTR) applications. By integrating thermogravimetric analysis, microstructural characterization (SEM/EDS), phase identification (XRD), and kinetic evaluation within a unified experimental framework, the present work enables a consistent assessment of oxidation resistance based on both qualitative and quantitative criteria.

The results demonstrate that 316L stainless steel exhibits the lowest oxidation resistance among the investigated materials. Oxidation at elevated temperatures is dominated by the formation of Fe-rich oxides, which are porous, poorly adherent, and prone to spallation. The relatively low parabolic rate constants and activation energy reflect weak diffusion barriers and limited long-term protective capability.

Incoloy 800H shows intermediate oxidation performance. A Cr_2O_3-based protective scale forms at temperatures up to approximately 1173 K, leading to diffusion-controlled parabolic oxidation behavior. However, at higher temperatures (≥ 1273 K), chromium depletion and the increasing formation of Fe-rich oxides result in scale thickening, increased porosity, and loss of adhesion. Consequently, despite exhibiting a relatively high apparent activation energy, the long-term oxidation resistance of Incoloy 800H is significantly reduced at very high temperatures.

Alloy 617 exhibits the most stable oxidation behavior within the investigated experimental conditions. It forms a continuous and adherent chromia-dominated oxide scale over a broader temperature range than the other alloys, resulting in lower parabolic rate constants and superior scale integrity. Although partial degradation and deviations from ideal parabolic kinetics are observed at 1473 K, Alloy 617 maintains comparatively better oxide scale stability.

The activation energy analysis confirms that oxidation kinetics are thermally activated and diffusion-controlled within the parabolic regime; however, activation energy alone should not be interpreted as a direct measure of oxidation resistance. Effective high-temperature oxidation resistance is governed by a combination of kinetic parameters, oxide scale morphology, phase stability, adhesion, and resistance to porosity and spallation. Differences in rate-controlling mechanisms at different

temperature regimes further limit the applicability of a single Arrhenius relationship across the entire temperature range.

The principal contribution of this work lies not in identifying general oxidation mechanisms, which are well documented in the literature, but in establishing a direct, quantitative, and application-oriented comparison of three candidate structural alloys using identical experimental conditions and a unified evaluation methodology.

Under the specific dry air and short-term isothermal oxidation conditions investigated, Alloy 617 demonstrates the most favorable combination of low oxidation kinetics and stable chromia-based scale formation. However, it is emphasized that actual VHTR service environments involve additional degradation mechanisms—including helium coolant impurities, carburization and decarburization, irradiation effects, and long-term exposure—which are beyond the scope of the present study. Therefore, the conclusions drawn here should be regarded as a comparative assessment of oxidation behavior under controlled air environments rather than a comprehensive evaluation of in-reactor performance.

Author Contribution H.U. designed the study, performed the experiments, analyzed the data, and wrote the initial draft of the manuscript. T.K.G. and S.L. supervised the research, contributed to the interpretation of results, and provided substantial feedback and revisions to the manuscript. All authors reviewed and approved the final manuscript.https://submission.springernature.com/new/submission/cf90c0a4-3444-4041-88f7-61e5940ce906/declarations.

Funding Open access funding provided by the Scientific and Technological Research Council of Türkiye (TÜBİTAK). This work has not received any funding, grants, or project support.

Data Availability No datasets were generated or analysed during the current study.

Declarations

Competing interests The authors declare no competing interests.

References

1. D. Buckthorpe, 1–Introduction to Generation IV nuclear reactors. In: Yvon P, ed. *Structural Materials for Generation IV Nuclear Reactors*. (Woodhead Publishing, 2017:1). https://doi.org/10.1016/B978-0-08-100906-2.00001-X.
2. K. L. Murty and I. Charit, *Journal of Nuclear Materials.* **383**, 2008 (189).
3. S. Ortner, *Frontiers in Nuclear Engineering*. **2**, 1253974 (2023).
4. P. J. Maziasz, *JOM* **70**, 2018 (66).

5. E. Romanczuk, K. Perkowski, and Z Oksiuta, *Materials* **12**, 3416 (2019).
6. G. Rogalski, A. Świerczyńska, M. Landowski, D. Fydrych, *Metals (Basel)*. **10**, 559 (2020).
7. V. Pauly, J. Kern, M. Clark, D. S. Grierson, K. Sridharan, *Wear Performance of Incoloy 800HT and Inconel 617 in Various Surface Conditions for High-Temperature Gas-Cooled Reactor Components* (2020).
8. H. M. Tawancy, *Engineering Failure Analysis* **110**, 2020 104402.
9. S. K. Mylavarapu, Development of Compact Heat Exchangers for very high-temperature gas-cooled reactors. *Ohio State University*. (2008).
10. H. Buscail, S. El Messki, F. Riffard, S. Perrier, and C. Issartel, *Oxidation of Metals* **75**, 2011 (27).
11. H. Mendoza, D. Angel, *High temperature stability of a 316 austenitic stainless steel coated with CeO2 nanoparticles*. (The University of Wisconsin Milwaukee, 2011).
12. F. Wang, Z. Zhang, G. Xiao, D. Zou, *Metals (Basel)* **15**, 347 (2025).
13. S. Zhang, D. Dong, Q. Wang, C. Dong, R Yang, *Metals (Basel)*. **11**, 213 (2021).
14. H. F. Lopez, H. Mendoza, and B. Church, *Metallurgical and Materials Transactions A Physical Metallurgy Materials Science* **45**, 2014 (1362).
15. E. Mondou, A. Proietti, C. Charvillat, et al., *Corrosion Science* **221**, 2023 111338.
16. H. Qi, Y. Qian, J. Xu, and M. Li, *Corrosion Science* **124**, 2017 (56).
17. J. Phother-Simon, T. Jonsson, and J. Liske, *Corrosion Science* **167**, 2020 108511.
18. Y. Liu, Y. Ning, Z. Yao, Y. Li, J. Zhang, and M. Fu, *Journal of Materials Research* **31**, 2016 (2164).
19. A. Kabir, D. Koszelow, T. Miruszewski, V. B. Tinti, V. Esposito, F. Kern, and S. Molin, *Advances in Science and Technology Research Journal* **18**, 2024 (10).
20. A. Qian, K. Zhuo, B. N. Choi, et al., *J Alloys Compd.* **688**, 2016 (814).
21. M. Haq and T. Naqvi, *Mater Today Proc.* **43**, 2021 (1977).
22. Z. Liu, G. Xu, Y. Zhang, L. Zhang, and J. Huang, *Materials Science and Engineering: A* **879**, 145282 (2023).
23. E. P. Ryklina, K. A. Polyakova, S. D. Prokoshkin, *Metals (Basel)* **11**, 119 (2021).
24. Y. Zhang, S. Wang, E. Lordan, K. Dou, X. Zhou, and T. Hashimoto, *Journal of Alloys and Componds* **895**, 2022 162219.
25. P. Yvon and F. Carré, *Journal of Nuclear Materials* 2009. https://doi.org/10.1016/j.jnucmat.2008.11.026.
26. J. Benz, R. Wright, and T. Lillo, Aging of Alloy 617 at 650 and 750 °C. Idaho National Laboratory Report, INL/EXT-12-27974, (2013).
27. D. Kim, C. Jang, and W. S. Ryu, *Oxidation of Metals* **71**, 2009 (271).
28. C. Jang, D. Kim, D. Kim, I. Sah, W. S. Ryu, and Y. S. Yoo, *Transactions of Nonferrous Metals Society of China (English Edition)*. **21**, 2011 (1524).
29. A. Kewther, M. S. J. Hashmi, and B. S. Yilbas, *Jounal of Materials Engineering Performance* **10**, 2001 (108).
30. M. Bates, *Exposure* 1 (1984).
31. I. Sah, D. Kim, H. J. Lee, and C. Jang, *Surface and Coatings Technology* **236**, 2013 (400).
32. Treatment H. HAYNES Waspaloy alloy alloy description : physical properties (2008)
33. S. K. Sharma, F. X. Li, G. D. Ko, and K. J. Kang, *Journal of Nuclear Materials* **405**, 2010 (165).
34. H. M. Tung and J. F. Stubbins, *Journal of Nuclear Materials* 2012. https://doi.org/10.1016/j.jnucmat.2012.01.015.
35. Kh. A. Al-Hatab, M. A. Al-Bukhaiti, and U. Krupp, *Appl Surf Sci.* **318**, 2014 (275).
36. M. Archana, Ch. J. Rao, S. Ningshen, and J. Philip, *J Mater Eng Perform.* **30**, 2021 (931).
37. D. Kim, G. Lee, S. J. Jeong, W. G. Kim, and J. Y. Park, *Nuclear Engineering and Technology* **43**, 2011 (429).
38. G. G. Lee, S. Jung, J. Y. Park, W. G. Kim, S. D. Hong, and Y. W. Kim, *Journal of Materials Science and Technology* **29**, 2013 (1177).
39. T. S. Jo, S.-H. Kim, D.-G. Kim, J. Y. Park, and Y. Kim, *Metals and Materials International* **14**, 2008 (739).
40. G.-G. Lee, S. Jung, D. Kim, Y.-W. Jeong, and D.-J. Kim, *Nuclear Engineering and Design* **271**, 2014 (301).
41. L. Xiao, W. Li, and G. Cota-Sanchez, *Nuclear Engineering and Design* **398**, 2022 111970.
42. W. Zheng, H. Li, B. Du, et al., *Progress in Nuclear Energy* **172**, 2024 105188.
43. C. Jang, D. Lee, and D. Kim, *International Journal of Pressure Vessels and Piping* **85**, 2008 (368).
44. W. R, R. S, *Journal of Pressure Vessel Technology, Transactions of the ASME*. 136, (2014).
45. R. Swindeman, *Journal of Pressure Vessel Technology* **136**, 054001 (2014).

46. Science N. Structural Materials for Advanced Nuclear Systems (2013).
47. M. F. Ashby, M. Smidman, Materials for Nuclear Power Systems. *Granta materials inspiration MFA* (2010).
48. K. Mo, G. Lovicu, H. M. Tung, et al., *Journal of Nuclear Materials.* **443**, 2013 (366–377).
49. W. S. Chen, W. Kai, L. W. Tsay, and J. J. Kai, *Nuclear Engineering and Design* **272**, 2014 (92).
50. L. Tan, T. R. Allen, and Y. Yang, *Corrosion Science* **53**, 2011 (703).
51. K. I. Choudhry, S. Mahboubi, G. A. Botton, J. R. Kish, and I. M. Svishchev, *Corrosion Science* **100**, 2015 (222).
52. Yang Z, Lu JT, Yuan Y, et al. *Materials at High Temperatures.* 34, 0 (2016).
53. H. Akhiani, M. Nezakat, M. Sanayei, and J. Szpunar, *Materials Science and Engineering A* **626**, 2015 (51).
54. Y. Cao and H. Di, *Materials Letters* **163**, 2016 (24).
55. AK Steel Corporation. Product Data Sheet: Stainless Steel 316/316L. 2, (2007).
56. International H. *Haynes 617 Alloy Description:Physical Properties Report* (2008).
57. Metals S. *INCOLOY Alloy 800 Report*. (2004).
58. S. Arrhenius, *Über die Reaktionsgeschwindigkeit bei der Inversion von Rohrzucker durch Säuren.* **4U**, 1889 (226).

Authors and Affiliations

Hakan Us[1] · Tushar K. Ghosh[2] · Sudarshan Loyalka[2]

✉ Hakan Us
hakanus@sinop.edu.tr

Tushar K. Ghosh
ghoshT@missouri.edu

Sudarshan Loyalka
LoyalkaS@missouri.edu

[1] Department of Nuclear Energy Engineering, Faculty of Engineering and Architecture, Sinop University, Sinop, Turkey

[2] University of Missouri, Columbia, MO, USA